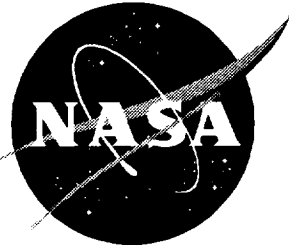# Assessment of an Euler-Interacting Boundary Layer Method Using High Reynolds Number Transonic Transport Flight Data

Daryl L. Bonhaus and Dal V. Maddalon
Langley Research Center, Hampton, Virginia

August 1998

Acknowledgment

The authors gratefully acknowledge the support of Javier A. Garriz, who generated the grids used in this study.

Contents

1. Summary

Flight-measured high Reynolds number turbulent-flow pressure distributions on a transport wing in transonic flow are compared to unstructured-grid calculations to assess the predictive ability of a three-dimensional Euler code (USM3D) coupled to an interacting boundary layer module. The two experimental pressure distributions selected for comparative analysis with the calculations are complex and turbulent but typical of an advanced technology laminar-flow wing. An advancing front method (VGRID) was used to generate several tetrahedral grids for each test case.

Initial calculations left considerable room for improvement in accuracy. Studies were then made of experimental errors, transition location, viscous effects, nacelle flow modeling, number and placement of spanwise boundary layer stations, and grid resolution. The most significant improvements in the accuracy of the calculations were gained by improvement of the nacelle flow model and by refinement of the computational grid.

Final calculations yield results in close agreement with the experiment. Indications are that further grid refinement would produce additional improvement but would require more computer memory than is available.

The appendix data compare the experimental attachment line location with calculations for different grid sizes. Good agreement is obtained between the experimental and calculated attachment line locations.

2. Introduction

2.1. Background

Code validation by comparison with flight test results is an important part of determining the accuracy and usefulness of a newly developed code. These comparisons can be very important in practical applications such as determining manufacturing tolerances of turbulent-flow aircraft or designing an entirely new laminar flow aircraft configuration. Industry users urge code developers to deliver user-friendly products tested and validated for everyday use.

Between 1986 and 1991, NASA and its industry partners completed a series of flight tests on various airplanes modified to obtain laminar flow (refs. 1 through 7). These tests culminated in the successful flight validation of the hybrid laminar-flow control (HLFC) concept at transonic speeds and high Reynolds numbers on both wings and nacelles (refs. 2 through 7). This concept involves a combination of active laminar-flow control (LFC) with suction from the leading edge to the front spar and passive laminar flow obtained by means of a favorable pressure gradient from the front spar to more rearward locations. During these experiments, a high-fidelity database was created that is useful for the validation of advanced computational fluid dynamics codes. The flight data used in this report were obtained on a modern transport airplane with high-bypass-ratio wing-mounted engines. One result of the flight experiments was the realization that the design procedure used for the wing surface pressure computations was often inadequate for predicting details of a complex pressure distribution. It was therefore decided to undertake a detailed study of the ability of an advanced aerodynamic code to predict three-dimensional experimental pressure distributions.

2.2. Objective

Flight-measured high Reynolds number turbulent-flow wing pressure distributions are compared to unstructured-grid calculations to assess the predictive ability of a three-dimensional Euler code (USM3D) coupled to an interacting boundary layer module. The transonic test points selected for analysis have pressure distributions that are complex and turbulent, yet typical of an advanced technology laminar-flow wing.

2.3. Technical Approach

The state of the art in computational fluid dynamics offers a variety of methods for computing aircraft aerodynamic performance. These methods range from simple linear methods to full Navier-Stokes simulations. When viscous effects are important (e.g., for a laminar-flow airplane), they must be included in the mathematical model used to compute the flow. In addition, the engineer must decide whether to use a structured or unstructured computational grid. The generation of grids suitable for computation of an inviscid flow is generally easier for unstructured-grid

methods, while structured-grid methods are generally more efficient in terms of both the computer memory requirements and the execution time of the flow solver.

The geometry in the present study is sufficiently complex to make generation of a block-structured grid costly and time-consuming. Any gains in solver efficiency would be small compared to the time required to generate a suitable grid. Such methods, however, are relatively mature and robust and efficiently provide viscous solutions once the grid is generated.

While unstructured-grid Navier-Stokes codes exist, the generation of unstructured grids suitable for high Reynolds number flows remains difficult. The grid must be highly stretched near solid boundaries to properly resolve the boundary layer without generating an unnecessarily large number of grid points in the streamwise and crossflow directions. Methods have been developed to produce grids of this type, but at present they lack the robustness required for widespread use.

The coupling of an inviscid unstructured-grid method with an interacting boundary layer model offers a good compromise for the present study. Inviscid unstructured-grid methods and grid generation techniques are well established and relatively robust. When coupled to a reasonable boundary layer model, an inviscid solver will capture most features of interest in an attached flow. For these reasons, the present work uses this method to analyze the aerodynamics of the configuration.

3. Nomenclature

C_L lift coefficient

C_p surface pressure coefficient

H altitude

HLFC   hybrid laminar flow control

IBL   interactive boundary layer

LE   leading edge

LFC   laminar flow control

M free-stream Mach number

MAC   mean aerodynamic chord

R free-stream Reynolds number based on mean aerodynamic chord

WBL   wing butt line

x/c chordwise coordinate, fraction of local chord

α angle of attack, deg

4. Overview of Experiment

The following sections present a description of the overall experiment. One wing of a modern high-bypass-ratio transport airplane was modified by removing the two slats closest to and outboard of the nacelle. The slats were replaced with a new suction leading-edge test article and a Krüeger flap. An extensive amount of experimental data was then obtained at many different flight test points that are representative of the operating conditions of a commercial airplane.

4.1. Test Article Description

Figure 1 shows a sketch of the perforated leading-edge test article with a sweep of approximately 25° that is mounted on the left wing of the airplane. The test article was 22.4 ft long and extended 25 in. from the leading edge to the front spar. Titanium sheet of 0.040-in. thickness was used for the perforated outer surface of the suction panel.

Four rows of 34 pressure taps each were installed outboard of the nacelle at wing butt lines (WBL's) 344, 389, 428, and 479 in. (fig. 1). Each row included 20 upper surface taps mounted in the leading-edge box suction panel. The taps did not penetrate the perforated titanium skin but terminated in a small cavity in the stringer beneath the skin. The resulting pressures measured on the leading-edge test article were thus relatively disturbance free. The 10 surface pressure measurements made in the sparbox region used strip-a-tube belts bonded to the wing surface. The forward edges of the belts were tapered to a wedge shape to reduce any flow disturbance. The most forward inspar pressure tap (e.g., 20 percent chord at WBL = 344 in.) was close to the initial wedge surface so that its pressure values might have been affected by flow acceleration over the wedge. A tapered plastic strip was

applied at the belt sides to help reduce flow disturbances further. The pressure belts terminated at the rear spar.

4.2. Test Cases

Two transonic high Reynolds number test cases were chosen for data analysis. The first had a more forward shock location with $M = 0.793$ and $\alpha = 2.598°$ ($C_L = 0.447$). The second had a more aft shock location with $M = 0.820$ and $\alpha = 2.377°$ ($C_L = 0.449$). Additional test characteristics for the two flight conditions are summarized in table 1.

The suction system was not used when measuring the pressures over the wing box. Thus, the flight data represent a turbulent wing flow in both cases.

5. Overview of Calculations

More detailed information concerning the computational method used for analysis of the configuration is presented in the following sections. First, the features of the flow solver and boundary layer model are described. Next, the method used to generate grids is outlined. Finally, some issues pertaining to the airplane geometry are discussed.

5.1. Code Description

The flow solver, referred to as a three-dimensional Euler code (USM3D) (refs. 8 through 10), computes the steady-state solution to the Euler equations on a grid of tetrahedral cells. Averages of conserved quantities (mass, momentum, and energy) are stored at the centroid of each cell. A cell-centered finite-volume formulation of Roe's flux difference splitting scheme is used to discretize the spatial derivatives. A red-black Gauss-Seidel scheme is used to integrate the equations in time to the steady-state solution.

To complete the specification of the solver, the boundary conditions used for the present calculations are given. On the wing, the normal velocity component is specified on the surface. On the fuselage, nacelle, pylon, and symmetry plane, flow tangency is enforced. In the far field, Riemann invariants are used to compute conserved quantities on the boundary. On the inlet and exit faces of the nacelle, conserved quantities are prescribed so that mass flow is conserved, and total pressure and total temperature within the simulated engine remain constant at free-stream conditions. The resulting nacelle flow is equivalent to that through an open duct.

5.2. Boundary Layer Model

The boundary layer on the wing is modeled as a set of two-dimensional strips at specified span locations. At each of these boundary layer stations, the surface pressure computed by USM3D is used as the boundary condition in a two-dimensional boundary layer code (ref. 11). The solution of the boundary layer code yields the displacement thickness that is used to compute a transpiration velocity at the surface. The computed transpiration velocities are bilinearly interpolated to the wing surface nodes between each pair of boundary layer stations and are then used as a boundary condition for USM3D. Input parameters allow specification of the number of flow solver iterations between boundary layer calculations.

The boundary layer code uses the Keller box method to solve a finite-difference discretization of the two-dimensional compressible boundary layer equations (ref. 11). By using the velocity and density at the edge of the layer, the density at the wall, and the displacement thickness computed by the boundary layer code, an equivalent transpiration velocity is computed via Lighthill's equation (ref. 12).

5.3. Computational Grids

The grid generation code used is referred to as VGRID (refs. 13 through 15) and is based on the advancing-front technique. The distribution of tetrahedra is governed by user-prescribed sources that influence the solution of a Poisson equation on an underlying Cartesian background grid. The placement of sources on this background grid allows clustering of cells near points of interest. The process begins with a triangulation of each surface patch of the geometry. From this triangulation (which forms the initial "front"), points are added to form cells according to the spacing specified on the background grid.

Several grids were generated during the course of this study, and the relevant parameters of each grid are summarized in table 2. Included in these parameters is

3

the grid spacing specified at various chord locations in the midspan region. The sequence of refinements represented by grids 1, 3, and 4 in table 2 is illustrated in figure 2, in which each surface grid is depicted in the region where the experimental data were measured (i.e., the midspan region of the wing). The chord regions targeted for refinement were chosen based on the experimental measurements. Illustrations of the triangulation of the entire airplane surface for the finest grid (grid 4 in table 2) are presented in figure 3. The overall size (i.e., number of tetrahedra) of the finest grids was constrained to be less than about 1.4 million cells, due to the memory limit (256 million words) of the computer when the implicit integration scheme is used.

The implementation of the coupling between USM3D and the interactive boundary layer model allows boundary layer calculations only on chordwise patch boundaries on the wing. The initial grid (grid 1 in table 2) had only 10 such boundaries along the span, as shown in figure 4, along with the spanwise locations of the experimental data. Early results suggested that more stations may be required, so each wing patch was split in the chordwise direction, resulting in a maximum of 18 boundary layer stations, as shown in figure 5.

5.4. Geometry

A pointwise description of the aircraft surface was supplied by the manufacturer. Because the wing structure was designed to match the specified geometry under a cruise loading, this geometry includes aeroelastic deflections of the wing.

The initial aircraft geometry exhibited some surface irregularities on a few of its surface patches. These patches were located on the pylon and on the fuselage near the wing leading edge (LE). Efforts were made during grid generation to smooth out this effect. These regions are not expected to have a significant impact on the results in the region of interest.

6. Results and Discussion

Figure 6 presents a pressure distribution typical of a laminar flow control wing. The relative complexity of this pressure distribution makes it a good test case for an advanced three-dimensional code. The desired

characteristics of the wing's pressure distribution include an initial rapid flow acceleration, a slight peak in the pressure distribution near the leading edge, followed by a long, mild acceleration and then an aft pressure recovery region. For applications such as correctly predicting the amount of laminar flow obtained over a wing's surface, precise pressure distribution predictions in some chord regions are critical. If the shock location is forward of the prediction, or if the leading-edge recompression is too steep or extends past the suction region, large regions of laminar flow could be lost.

The first calculations performed with the initial grid (grid 1) and an early version of USM3D coupled to the boundary layer model are compared to the experimental data in figures 7 and 8 at Mach numbers of 0.793 and 0.820, respectively. Difficulty in accurately predicting pressures in regions critical to the design of a laminar-flow wing is evident at six different chord locations (x/c locations are specified for the 52-percent span location) as shown in the table.

x/c	Location
0.00 to 0.04	Leading-edge favorable pressure gradient
0.04 to 0.10	Leading-edge recompression
−0.10	Leading-edge constant pressure
0.10 to −0.30	Midchord favorable pressure gradient
−0.40	Midchord shock location
0.40 to 0.50	Midchord recompression after shock

There may also be an overcompression near the leading edge (e.g., fig. 8, 64 percent span). The calculations of figures 7 and 8 are clearly inadequate. To obtain a better fit between experiment and prediction, angle of attack is often changed to match another parameter such as lift coefficient. In this work, the experimentally measured angle of attack is always used. Efforts to improve solution accuracy are documented in the following sections.

6.1. Effect of Experimental Errors

The maximum experimental errors in Mach number and angle of attack were estimated to be ±0.002 and ±0.25°, respectively. Figure 9 shows the combined effect of these potential errors by applying the positive and negative error extremes to the given flight

4

conditions at $M = 0.793$ on grid 1. The two calculations do not bracket the experimental data; therefore, the disagreement with the experimental data cannot be due solely to experimental error.

A higher Mach number would improve the agreement between code and experiment. To determine the effect of Mach number alone, the $M = 0.793$ calculation was repeated with $M = 0.795$. The results are given in figure 10 where it is seen that this small change in Mach number has an almost negligible effect on the pressure distribution.

The $M = 0.793$, $\alpha = 2.598°$ calculation was repeated with $\alpha = 2.848°$ on grid 1 to determine the effect of angle-of-attack error alone. The results are given in figure 11 where it is seen that this change provides better agreement in the midchord region but not in the leading-edge recompression region (see fig. 11 inset). On the basis of these and subsequent results on a refined grid (appendix A), it is concluded that the discrepancy between code and experimental data is not due to an angle-of-attack error of 0.25°.

6.2. Effect of Transition Location

The previous calculations assume that boundary layer transition occurs at the wing leading edge. A transition front at 42 to 47 percent chord (the measured transition location for the four experimental span stations with the suction system active) was specified in the input to the code for these stations on grid 1. The results are given in figure 12; they show that this variation in the exact transition location has a negligible effect on the prediction. This issue is revisited in appendix A on a refined grid.

6.3. Effect of Boundary Layer

Inclusion of boundary layer effects can have a profound impact on the wing pressure distribution. In figure 13, calculations on grid 1 with and without the boundary layer model are presented with the experimental data. As expected, the inviscid solution exhibits a shock farther aft than does the viscous solution. The inviscid solution appears to be in slightly better agreement with the experimental data than the viscous solution. Since all schemes for solving the Euler equations contain numerical dissipation that decreases as the grid is refined, this agreement is typically an indi-

cation that the grid is too coarse. The effect of grid refinement is investigated in section 6.7.

6.4. Effect of Nacelle Flow Modeling

Using a new version of USM3D was necessary to overcome a hard-coded limit of 10 boundary layer stations in the initial code. This new version also included improvements resulting in more physically correct nacelle inlet and exit boundary conditions. In the original code, the Mach number at the exit of the engine is set to the free-stream Mach number, while the Mach number at the engine inlet face is adjusted so that mass flow is conserved through the engine. The newer code uses a more physically correct approach (described in ref. 16) in which quantities are set on the inlet and exhaust faces of the engine based on the directions of characteristic lines at these faces. This model allows specification of stagnation conditions in the engine and hence simulation of propulsion effects. For the cases presented in this work, the conditions specified in the engine were those of the free stream; therefore, no propulsion effects are simulated.

Figure 14 shows a comparison of the results obtained on grid 1 by using the initial and the improved versions of USM3D. By using the older nacelle model, the Mach number at the inlet was subsonic and less than the free-stream Mach number. The newer nacelle model yielded a slightly supersonic Mach number at the inlet face due to the slight contraction and reexpansion of the diffuser cross section upstream of the inlet face. This difference in inlet flows has a dramatic impact on the mass flow captured by the engine and hence the disturbance of the surrounding flow field. Both the shock location and the leading-edge pressures are significantly improved by using the new code, although there is still much room for improvement. The improved nacelle boundary conditions are used for all remaining calculations on grids 2 through 5.

6.5. Effect of Number of Spanwise Boundary Layer Stations

The number of spanwise boundary layer stations needed for an accurate prediction of the experimental data was investigated by calculating the wing pressure distribution by using 4, 10, 14, 16, and 18 stations with grid 2 at $M = 0.793$. As grid 1 was limited to

5

10 spanwise boundary layer stations, a new grid (grid 2 in table 2) with the capacity for 18 boundary layer stations was used in these calculations. The results are presented in figure 15. Four stations alone are clearly inadequate and result in a pressure distribution closer to the inviscid solution. (The inviscid solution is not shown.) (Also see fig. 13.) The data prediction using 10 stations is nearly as good as the prediction using 18 stations (data for 14 and 16 stations are indistinguishable from the 18-station calculation). We conclude that the number of spanwise boundary layer stations is clearly an important factor but that the number need not be excessive.

6.6. Effect of Station Placement

Figure 16 shows the effect of the placement of the spanwise boundary layer stations on the computed pressure distribution. In both cases, the number of boundary layer stations and the grid resolution are fixed. For the calculation denoted as "with experimental stations," the set of boundary layer stations included the precise spanwise experimental data stations (stations 7, 9, 10, and 11 in fig. 5). For the calculation denoted as "without experimental stations," the boundary layer data were interpolated to the experimental data stations. As there is very little difference in the computations, we conclude that placement of the boundary layer stations is not critical.

6.7. Effect of Grid Refinement

The inviscid calculation of figure 13 agreed with the experiment better than did the viscous solution, and a lack of grid resolution was suspected (see also section 6.3). Based on the experimental data, grid 2 was refined near the leading edge and near the shock, yielding grid 3 (table 2 and fig. 2). The impact of this refinement is visible in figure 17, which compares results on grids 2 and 3. Note the sharper resolution of the shock, its better agreement with the experiment, and the appearance of a postshock expansion in the calculation that agrees well with the experimental data.

The improved agreement with experimental data obtained with grid 3 suggested that additional accuracy in the critical leading-edge region could be obtained with further grid refinement; however, grid 3 already required the maximum available computer memory. Additional refinement required other regions of the grid to be coarsened. Thus, two new grids (grids 4 and 5) were generated and are described in table 2. Grid 4 further refines the leading-edge region of grid 3 while coarsening the fuselage, nacelle, and wing trailing edge; grid 5 was generated to assess the effects of this coarsening.

Computed pressures on grid 4 for $M = 0.793$ are shown in figure 18 in comparison with results on grid 3. Some improvement of the prediction in the leading-edge region is apparent at the 46-percent and 52-percent span stations. At this level of grid resolution, the code is beginning to predict the higher order variations of the experimental pressure distribution that occur just downstream of the leading-edge peak C_p. The predicted shock location and pressures downstream of the shock are in excellent agreement with the experimental data. The midchord pressure distribution prediction is reasonable, but the disagreement with experimental data is still not fully explained.

Figure 19 shows results on grid 5 in comparison with those on grid 3 to assess the effects of coarsening the fuselage and nacelle. Note that there is no significant loss of accuracy in the regions of primary interest (i.e., the region where experimental data are available); however, significant loss of accuracy does occur near the trailing edge of the airfoil.

To illustrate the overall effect of the grid refinements in this study, calculations on grids 2 and 4 are presented in figures 20 and 21 for flight Mach numbers of 0.793 and 0.820, respectively. Improvement in the agreement of the prediction with experimental data is seen in regions where the earlier calculations were somewhat inaccurate.

A comparison of isobar patterns for the two flight conditions is also shown in figures 22 and 23. Computations are shown on grid 1 by using the original nacelle flow model and on grid 4 by using the improved nacelle model. Note the relatively parallel isobars in the redesigned hybrid laminar-flow wing section (located between the two vertical lines) just outboard of the nacelle. The strong influence of the nacelle pylon on the upper wing surface flow is also evident in these figures.

Appendix B compares the experimental attachment line location with calculations using grids 1

and 4. The results on grid 4 show good agreement with the experimental data near the attachment line.

Based on the sequence of results presented in the preceding sections, further refinement of the grid can reasonably be expected to produce further improvements in solution fidelity when sufficient computer resources are available.

7. Concluding Remarks

Initial calculations did not agree well with experimental data in six regions of the wing chord. To improve calculation accuracy, studies were made of discrepancies between computation and experiment arising from experimental uncertainties, specification of transition location, viscous effects, nacelle flow model, number and placement of spanwise boundary layer stations, and grid resolution. It was determined from these studies that uncertainties in the Mach number and angle-of-attack measurements were not significant contributors to the initial disagreement between calculations and experimental data. It was also determined that 10 boundary layer stations were sufficient to capture the pressure distribution.

Availability of flight data was invaluable in guiding the calculations. The first refinement of the inviscid grid (from grid 2 to grid 3) resulted in very little change in the pressures in the leading-edge region, and it is unlikely that further refinement would have been done solely on the basis of the computed results. The experimental data, however, indicated subtle variations in the leading-edge surface pressures that the calculation on the refined grid (grid 3) did not capture.

On this basis, the second refinement (from grid 3 to grid 4) was performed.

Improvement of the nacelle flow model had the largest single impact on the accuracy of the pressure distributions. Of particular importance is the 10-percent chord rearward movement of the shock due to the change in nacelle flow modeling. The upper surface rooftop Mach number increased by approximately 0.05, and the pressures near the leading edge were greatly improved.

Refinement of the inviscid grid also had a significant impact on accuracy. Two refinements of the inviscid grid concentrating primarily on the leading-edge region resulted in significantly improved calculations of the leading-edge pressures, the shock location and definition, and the pressures downstream of the shock. Reduction of the grid spacing at the leading edge by approximately 70 percent to 0.05 percent of the mean aerodynamic chord (MAC) was required to achieve good agreement between the calculations and experiment in five of six chord regions where the initial calculations were in poor agreement. The improved grids, however, were unable to capture the small local pressure gradients occurring in the leading-edge region of the outboard data stations. Further grid refinement is required to obtain these details; however, the limits of current computer resources were used in this study. A solution on a grid of 1 250 233 cells (grid 4) required 256 million words of memory and approximately six hours of processing time on the Cray C90 computer.

NASA Langley Research Center
Hampton, VA 23681-2199
April 1, 1998

7

Appendix A

Effect of Angle-of-Attack Errors, Transition Location, and Viscous Effects on a Refined Grid

Several calculations were repeated for the $M = 0.793$ case on grid 4 to confirm conclusions drawn from results obtained on grid 1.

The first case represents an increment in angle of attack of 0.25° to determine the effect of a maximum angle-of-attack error. The results are given in figure 24 and show that the increased angle-of-attack prediction is worse at the leading edge and that the shock is predicted to be aft of its true location. This result confirms the conclusion drawn in section 6.1 that discrepancies between experimental data and computations were not due to an experimental error in angle-of-attack measurement.

Figure 25 shows the results obtained by specifying a transition front at 42 to 47 percent chord in the midspan region. Although the corresponding calculation on grid 1 (fig. 12) was virtually identical to the fully turbulent result, the transitional case on grid 4 shows less agreement with the experiment than with the fully turbulent case. Because the experimental data were taken with the flow fully turbulent, it is expected that the fully turbulent calculation will provide the best prediction.

In figure 26, calculations with and without the boundary layer model are presented for grid 4. The same behavior noted in section 6.3 (fig. 13) is present in that the inviscid solution exhibits a shock well aft of the shock location of the viscous solution. However, in figure 26, the viscous result is in much better agreement with the experiment than is the inviscid result. The reduction of numerical dissipation due to grid refinement has moved the shock aft in both the inviscid and viscous solutions shown in figure 26.

Appendix B

Comparison of Experimental and Calculated Attachment Line Location for Two Grids

Detailed study of wing boundary layer flow, including transition prediction and stability analysis, often requires nearly exact knowledge of the attachment line location. It is therefore of interest to compare experimental and analytical results for the attachment line and also to see whether and how the grid size used might affect the location of the attachment line. Results in figures 27 and 28 for the four span locations of this study show that grid 4 does a better job of predicting the upper surface pressures near the highlight. The experimental attachment line location for the present conditions is near the highlight and agrees well with the grid 4 prediction. The predicted attachment line location is within 0.4 in. for the two grid sizes used in this study (table 2), but it is noted that the predicted attachment line may fall on opposite sides of the highlight, depending on the grid.

References

1. Wagner, R. D.; Maddalon, D. V.; Bartlett, D. W.; and Collier, F. S., Jr.: *Fifty Years of Laminar Flow Flight Testing*. SAE Paper 881393, Oct. 1988.

2. Maddalon, Dal V.; and Braslow, Albert L.: *Simulated-Airline-Service Flight Tests of Laminar-Flow Control With Perforated-Surface Suction System*. NASA TP-2966, 1990.

3. Maddalon, D. V.; and Wagner, R. D.: Boeing 757 Hybrid Laminar-Flow Control Flight Tests. *Langley Aerospace Test Highlights, 1990*. NASA TM-104090, 1990.

4. Maddalon, D. V.: Hybrid Laminar-Flow Control Flight Research. *Research Technology, 1991—Langley Research Center*. NASA TM-4331, 1991.

5. Williams, Louis J.; Hessenius, Kristin A.; Corsiglia, Victor R.; Hicks, Gary; Richardson, Pamela F.; Unger, George; Neumann, Benjamin; and Moss, Jim: *NASA Aerodynamics Program*. NASA TM-4368, 1992.

6. Wagner, R. D.; Maddalon, D. V.; Bartlett, D. W.; Collier, F. S., Jr.; and Braslow, A. L.: Laminar Flow Flight Experiments—A Review. *Natural Laminar Flow and Laminar Flow Control*, Springer Verlag, 1992, pp. 23–71.

7. Bhutiani, P. K.; Keck, D. F.; Laht, D. J.; and Stringas, M. J.: Investigating the Merits of a Hybrid Laminar Flow Nacelle. *The Leading Edge*, General Electric Co., 1993, pp. 32–35.

8. Smith, W. D.: Improved Pressure and Lift Predictions in Transonic Flow Using an Unstructured Mesh Euler Method With an Interacting Boundary Layer. M.S. Thesis, George Washington Univ., July 1994.

9. Parikh, Paresh; Pirzadeh, Shahyar; and Frink, Neal T.: Unstructured Grid Solutions to a Wing/Pylon/Store Configuration Using VGRID3D/USM3D. AIAA-92-4572, Aug. 1992.

10. Frink, Neal T.: Recent Progress Toward a Three-Dimensional Unstructured Navier-Stokes Flow Solver. AIAA-94-0061, Jan. 1994.

11. Cebeci, T.; Lee, K.; Clark, R. W.; Chang, K. C.; and Halsey, N. D.: Airfoils With Separation and the Resulting Wakes. *J. Fluid Mech.*, vol. 163, Feb. 1986, pp. 323–347.

12. Lighthill, M. J.: On Displacement Thickness. *J. Fluid Mech.*, vol. 4, pt. 4, 1958, pp. 383–392.

13. Parikh, Paresh; Pirzadeh, Shahyar; and Loehner, Rainald: *A Package for 3-D Unstructured Grid Generation, Finite-Element Flow Solution and Flow Field Visualization*. NASA CR-182090, Sept. 1990.

14. Pirzadeh, Shahyar: Structured Background Grids for Generation of Unstructured Grids by Advancing Front Method. AIAA-91-3233, Sept. 1991.

15. Pirzadeh, Shahyar: Recent Progress in Unstructured Grid Generation. AIAA-92-0445, Jan. 1992.

16. Hartwich, Peter M.; and Frink, Neal T.: Estimation of Propulsion-Induced Effects on Transonic Flows Over a Hypersonic Configuration. AIAA-92-0523, Jan. 1992.

Table 1. Summary of Flight Conditions and Geometry for Experimental Data

Parameter	Case 1	Case 2
Mach number	0.793	0.820
Angle of attack, deg	2.598	2.377
Altitude, ft	34 417	37 176
Reynolds number based on MAC	31.9×10^6	30.0×10^6
Lift coefficient	0.447	0.449
Sonic pressure coefficient	−0.455	−0.379
Span stations, percent	46, 52, 57, 64	
Semispan, in	750	
MAC, in	200	

Table 2. Summary of Grids Used in Calculations

Grid	Global statistics			Average spacing in test region, percent MAC, at nominal x/c—				Description
	Cells	Nodes (total)	Boundary nodes	0	0.15	0.5	1	
1	891 987	164 876	25 388	0.167	0.251	1.672	0.836	Initial grid, 10 IBL stations
2	895 759	165 647	25 618	0.167	0.251	1.672	0.836	Expanded to 18 IBL stations
3	1 341 188	244 211	30 079	0.134	0.251	1.338	0.836	Refined leading-edge and midchord region
4	1 250 233	229 052	31 724	0.050	0.084	1.338	1.672	More leading-edge refinement, coarsened fuselage and nacelle
5	598 243	110 510	16 761	0.134	0.251	1.338	1.672	Coarsened fuselage and nacelle without leading-edge refinement

11

Pressure belts

0.0002-in. diameter (nominal)
pressure inlets
(nonintrusive)

(a) Planform view.

Strip-a-tube belts
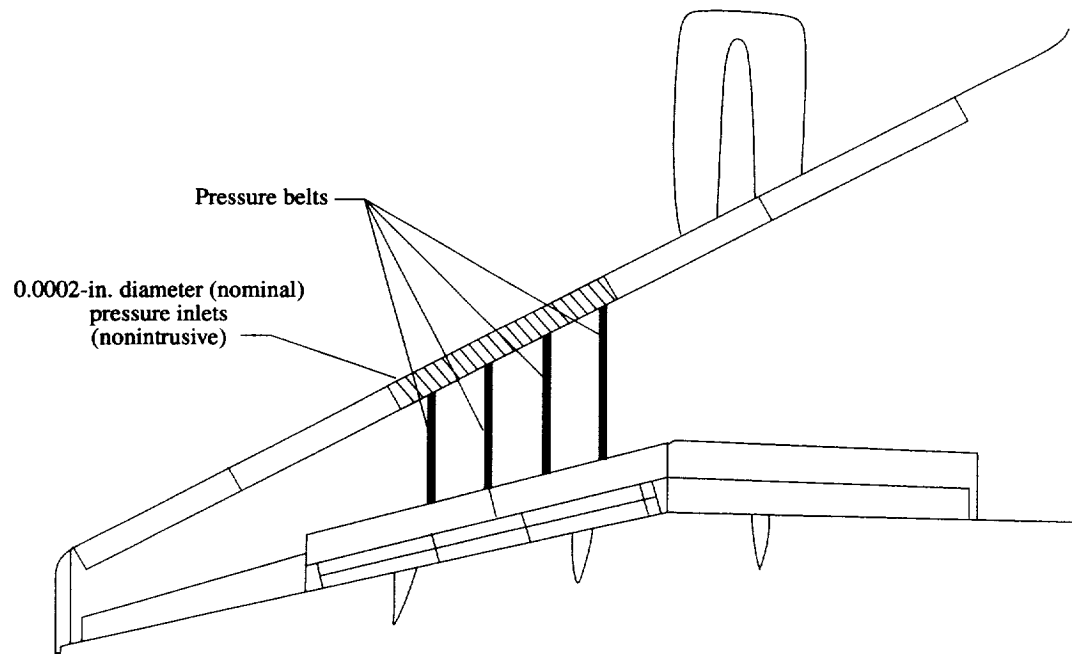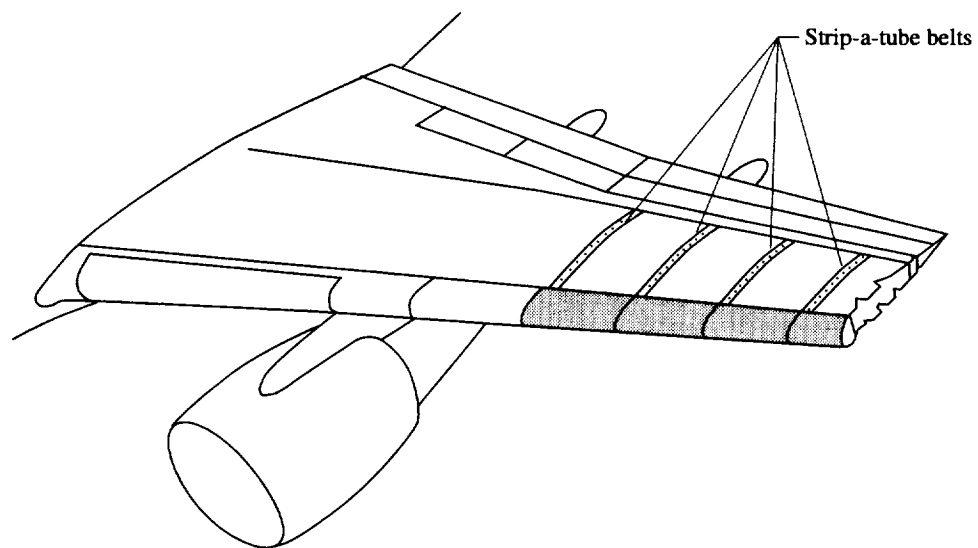
(b) Oblique view.

Figure 1. Leading-edge test article and pressure belt locations on wing surface.
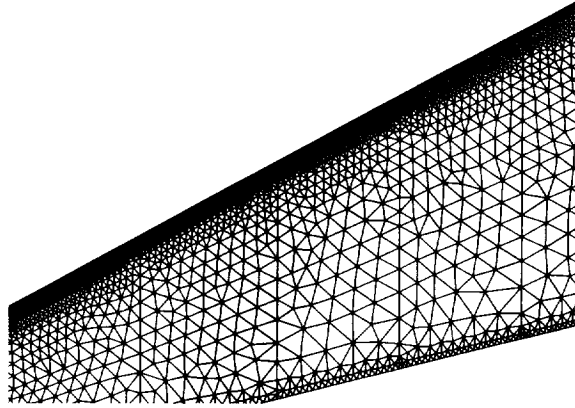
(a) Grid 1.
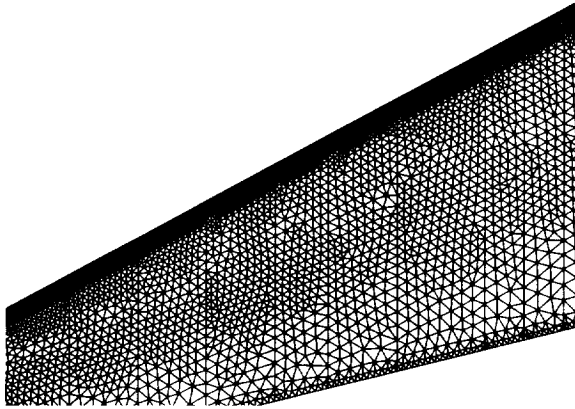
(b) Grid 3.
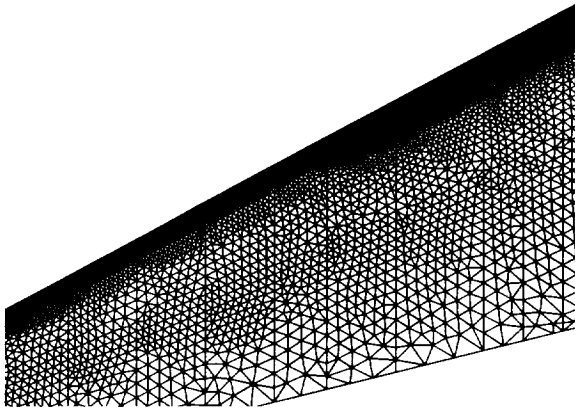
(c) Grid 4.

Figure 2. Test surface grid refinement.
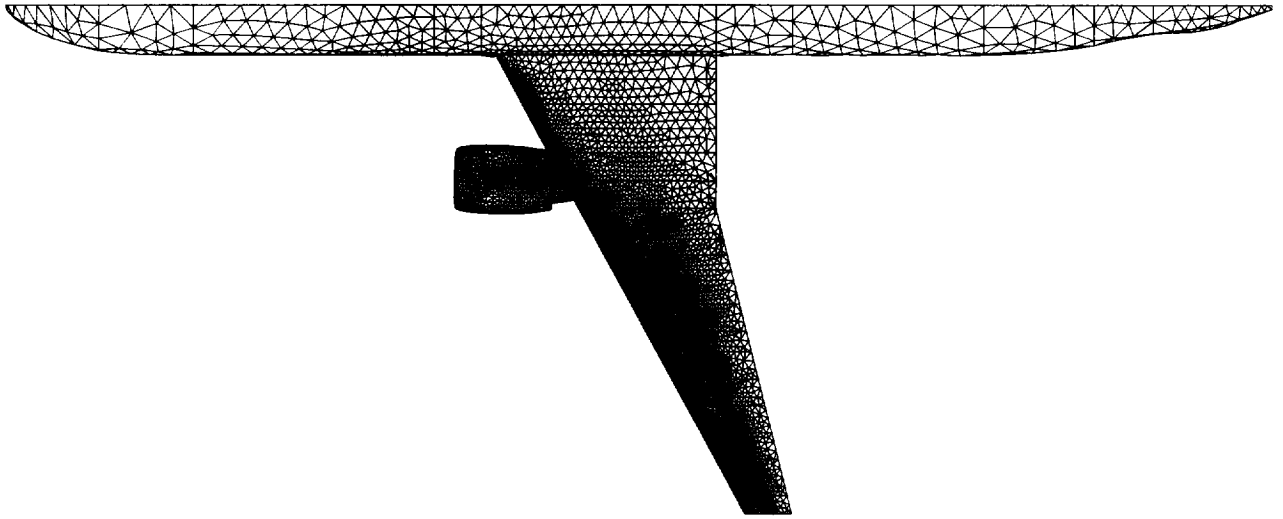
(a) Aircraft surface.
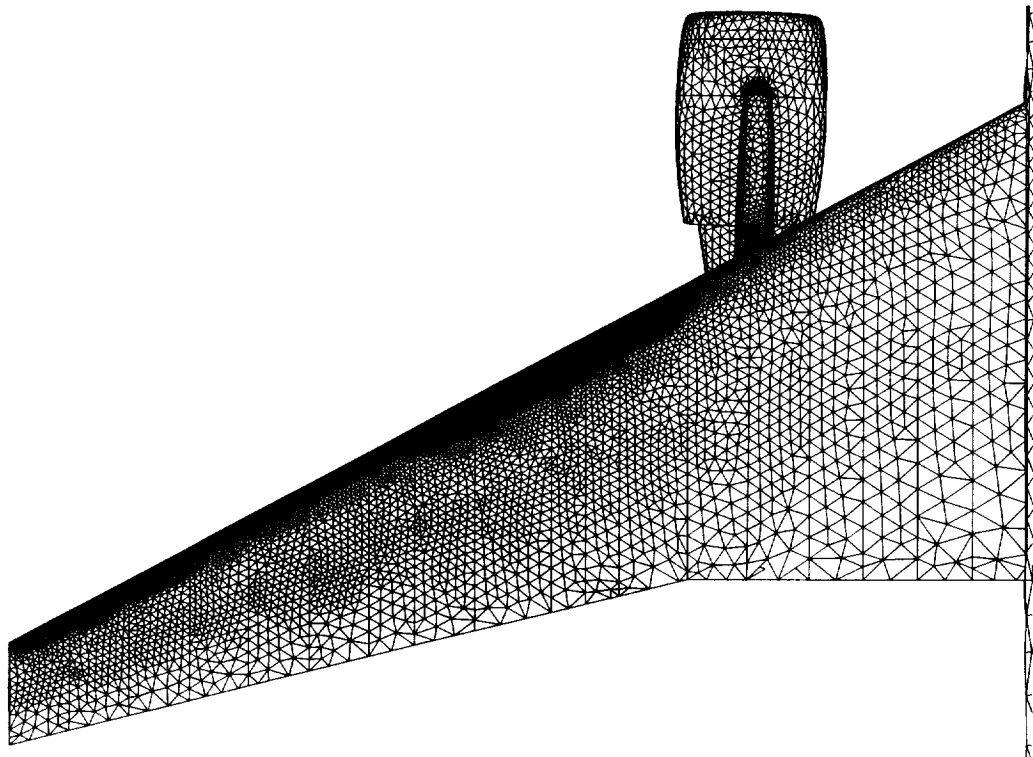
(b) Wing and nacelle.

Figure 3. Surface triangulation of aircraft geometry (grid 4).

14
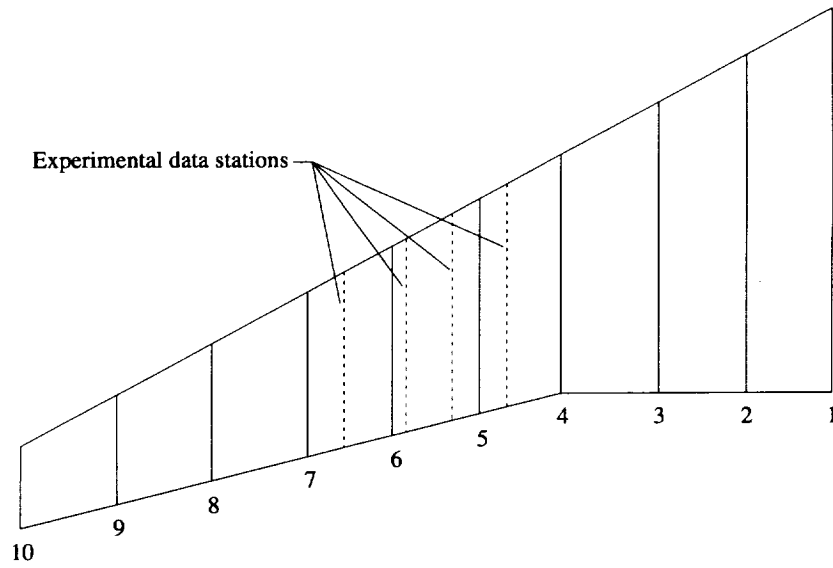
Figure 4. Boundary layer station locations for grid 1.
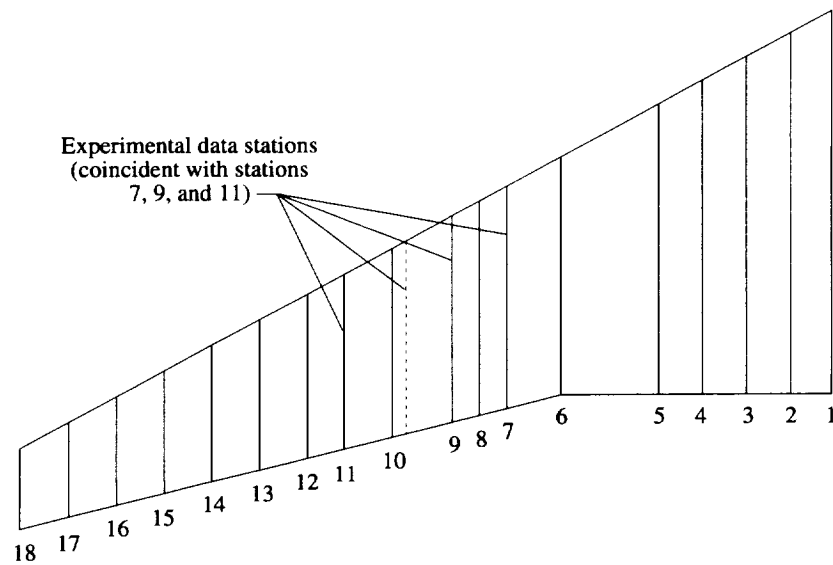
Figure 5. Boundary layer station location for grids 2 to 5.
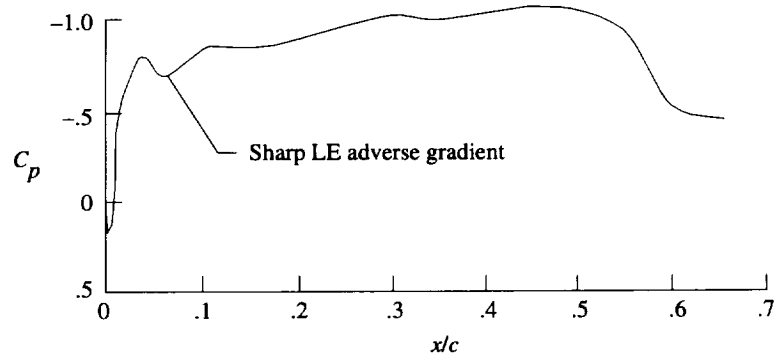
Figure 6. Pressure distributions typical of laminar-flow wing.

15
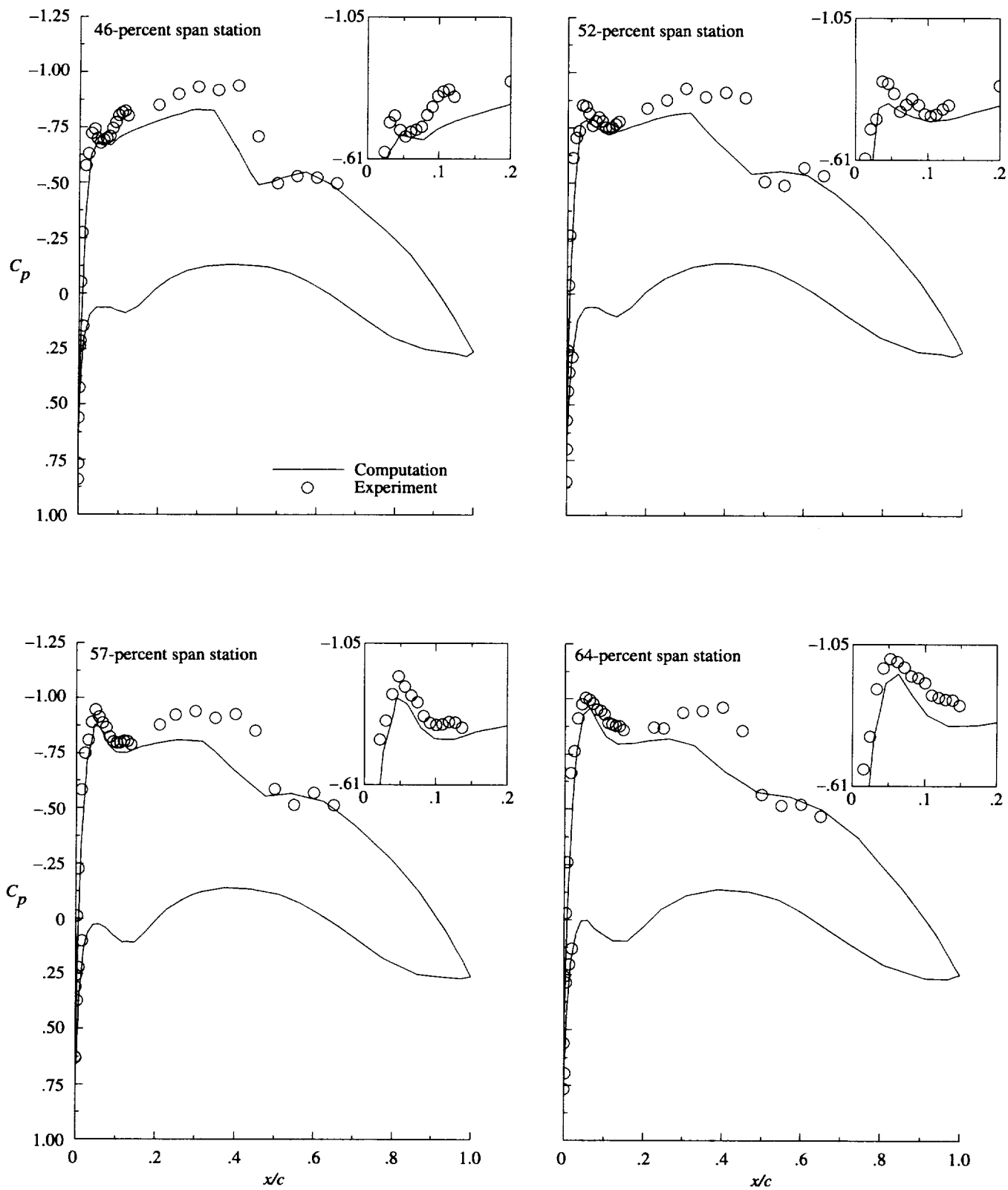
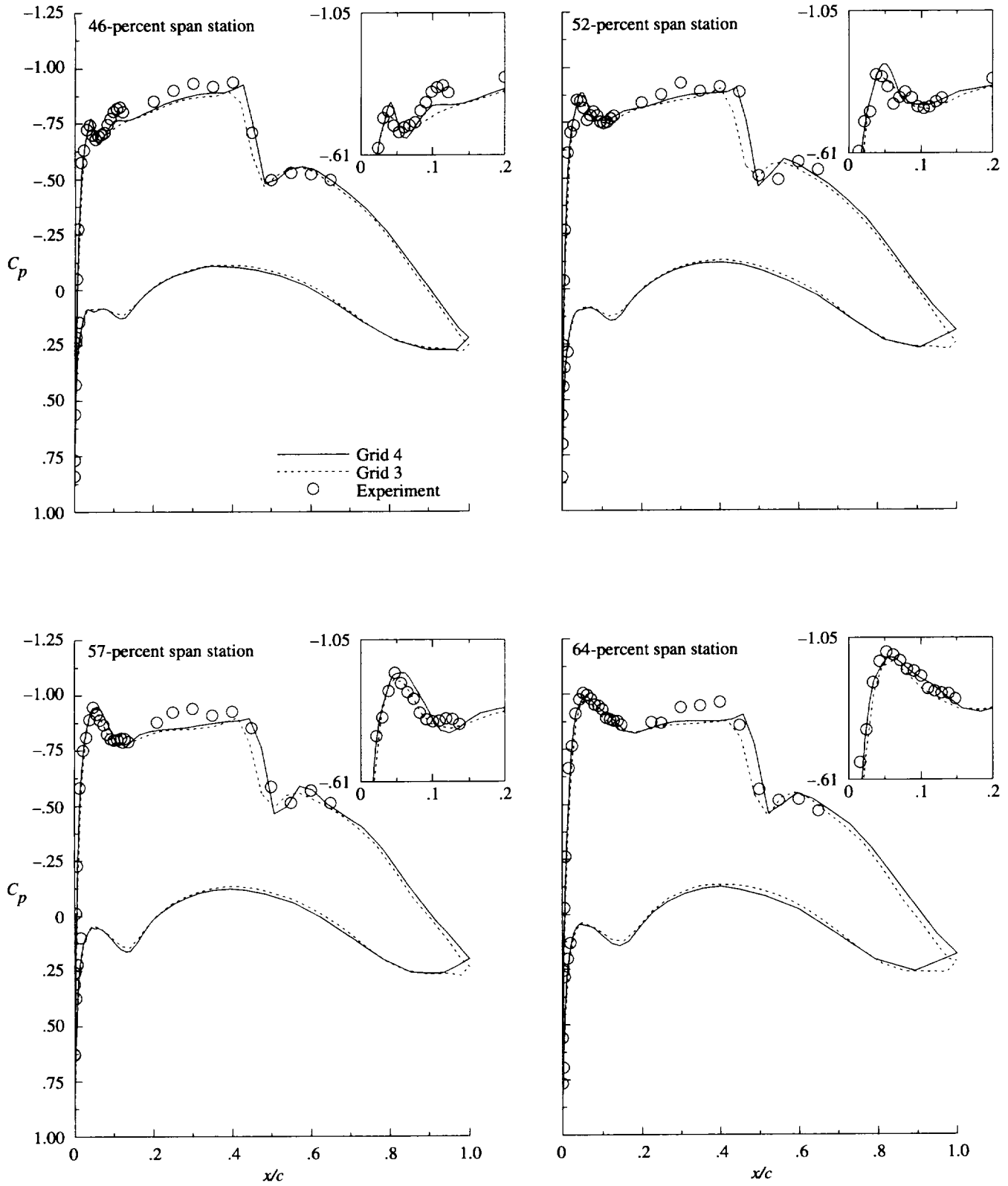Figure 7. Comparison of surface pressure coefficient with experiment for grid 1 ($M = 0.793$; $\alpha = 2.598°$; $R = 31.9 \times 10^6$; 10 IBL stations).
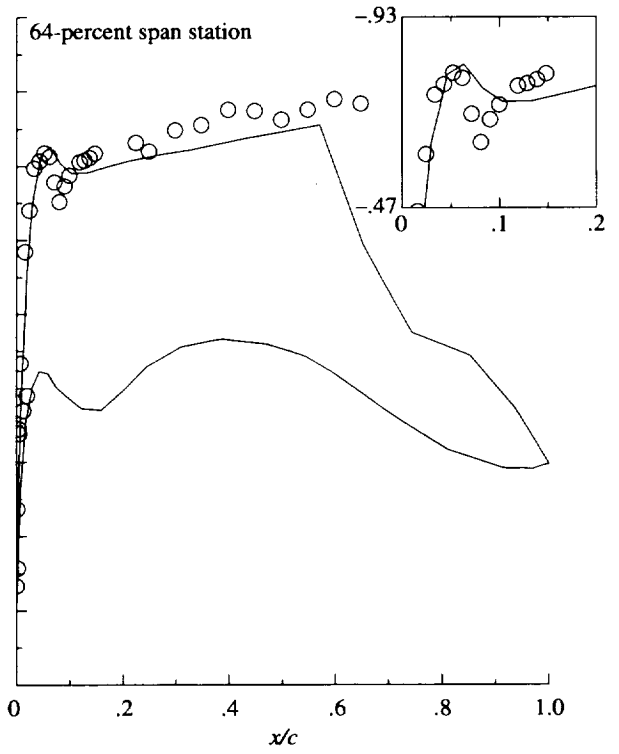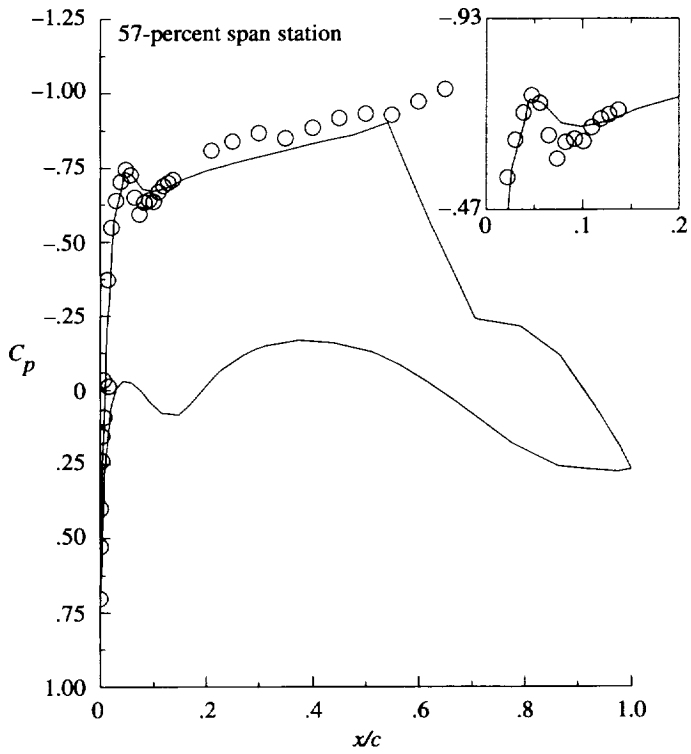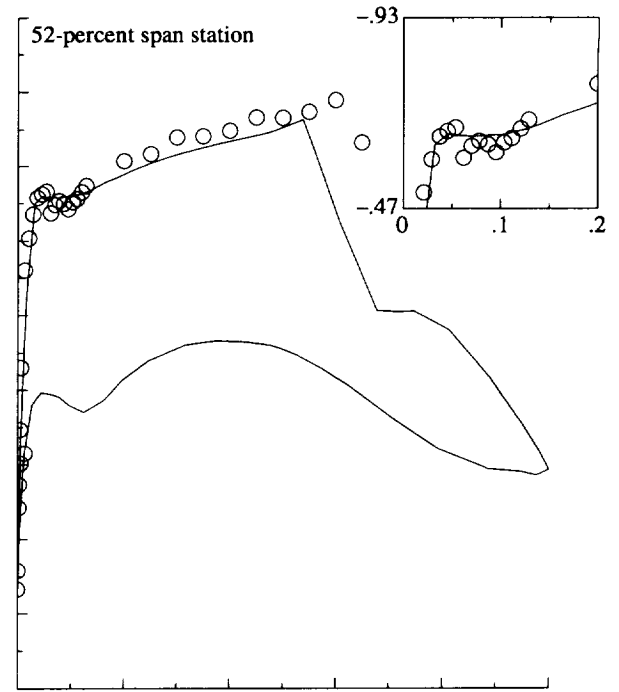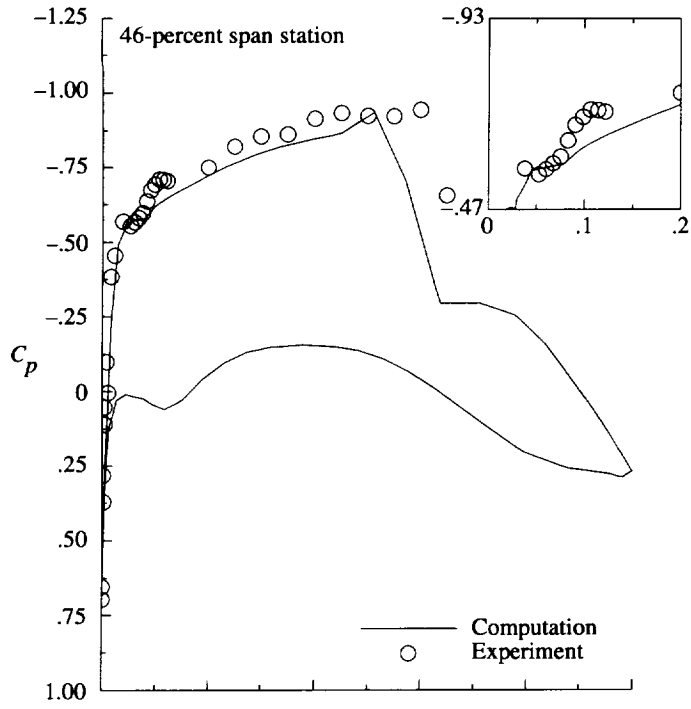
Figure 8. Comparison of surface pressure coefficient with experiment for grid 1 ($M = 0.820$; $\alpha = 2.377°$; $R = 30 \times 10^6$; 10 IBL stations).
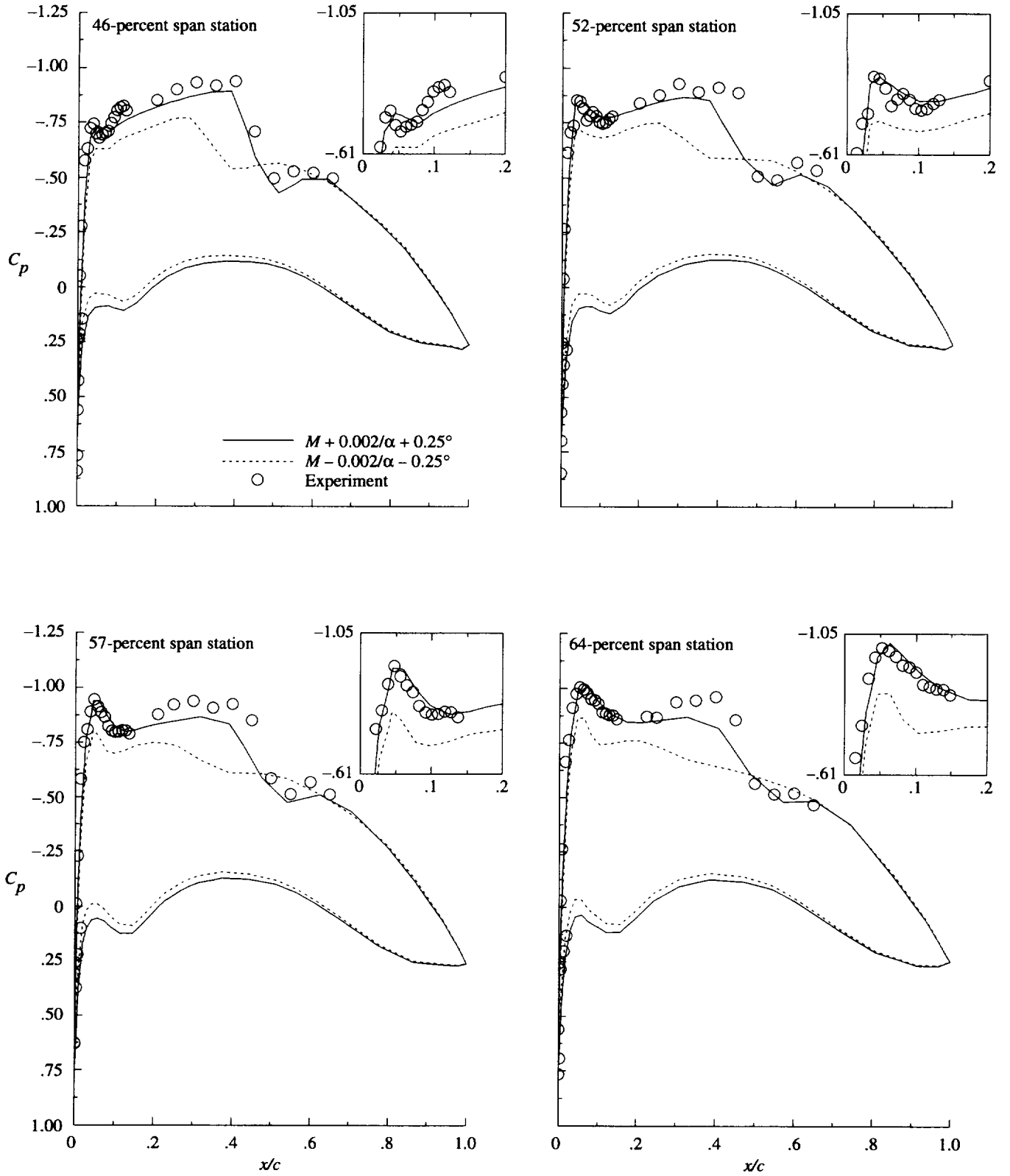
Figure 9. Combined effect of potential experimental Mach number and angle-of-attack errors on surface pressure coefficient distribution on grid 1 ($M = 0.793$; $\alpha = 2.598°$; $R = 31.9 \times 10^6$; 10 IBL stations).
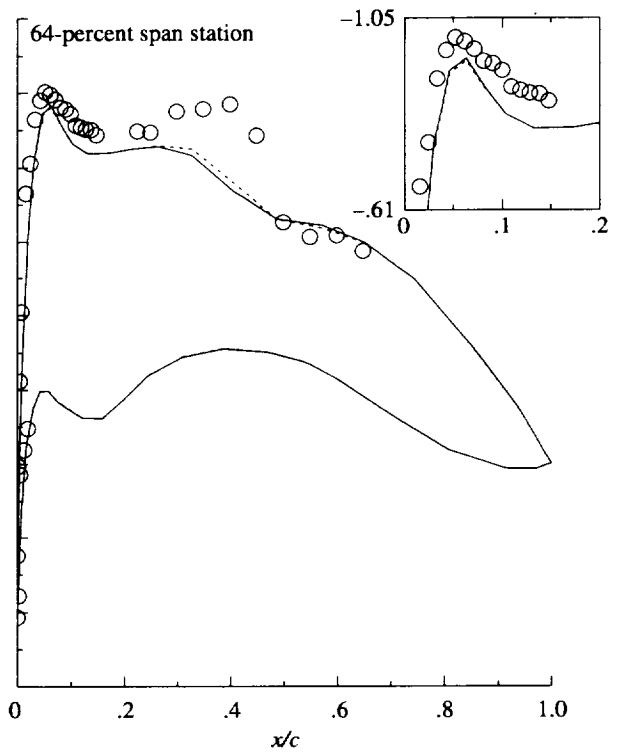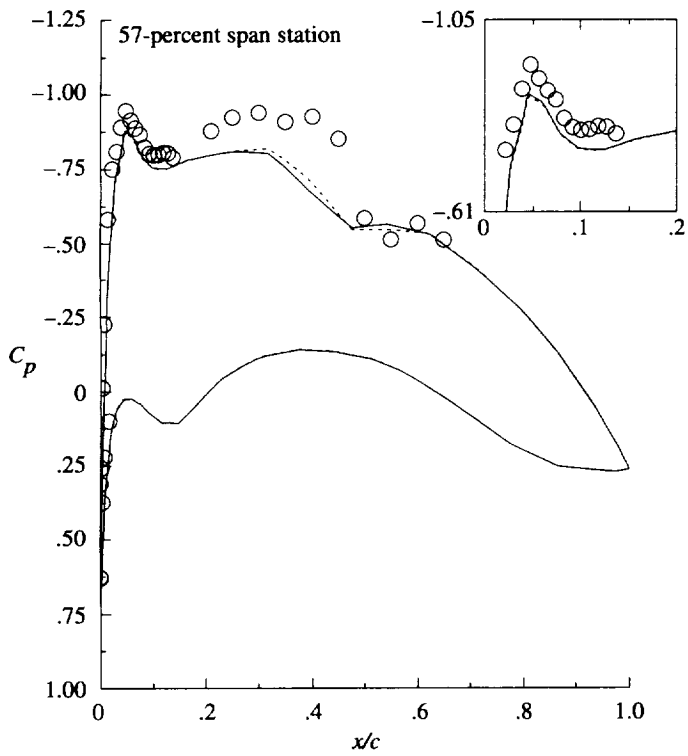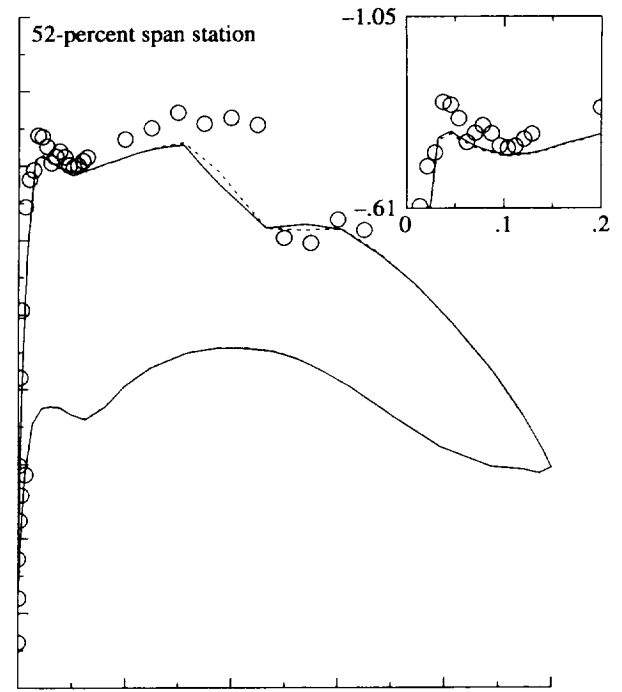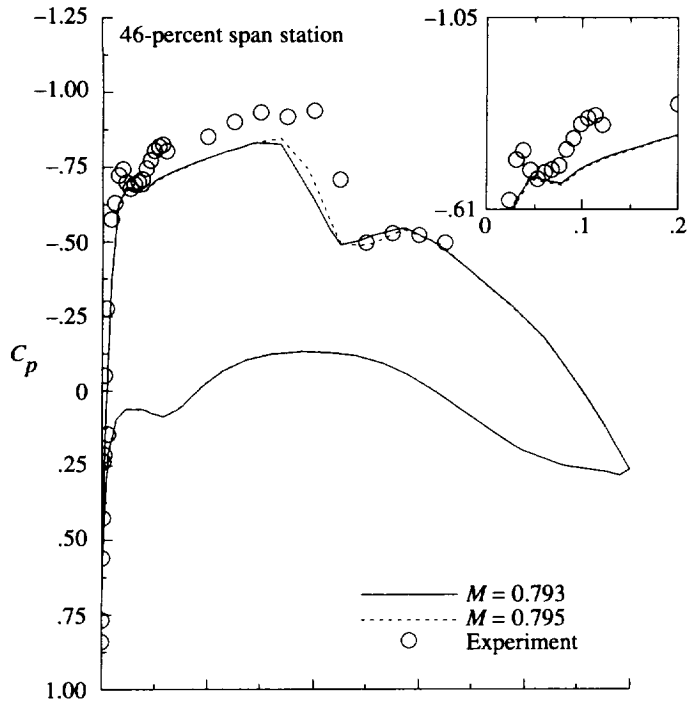
Figure 10. Effect of potential experimental Mach number error on surface pressure coefficient distribution on grid 1 (M = 0.793; α = 2.598°; R = 31.9 × 10^6; 10 IBL stations).
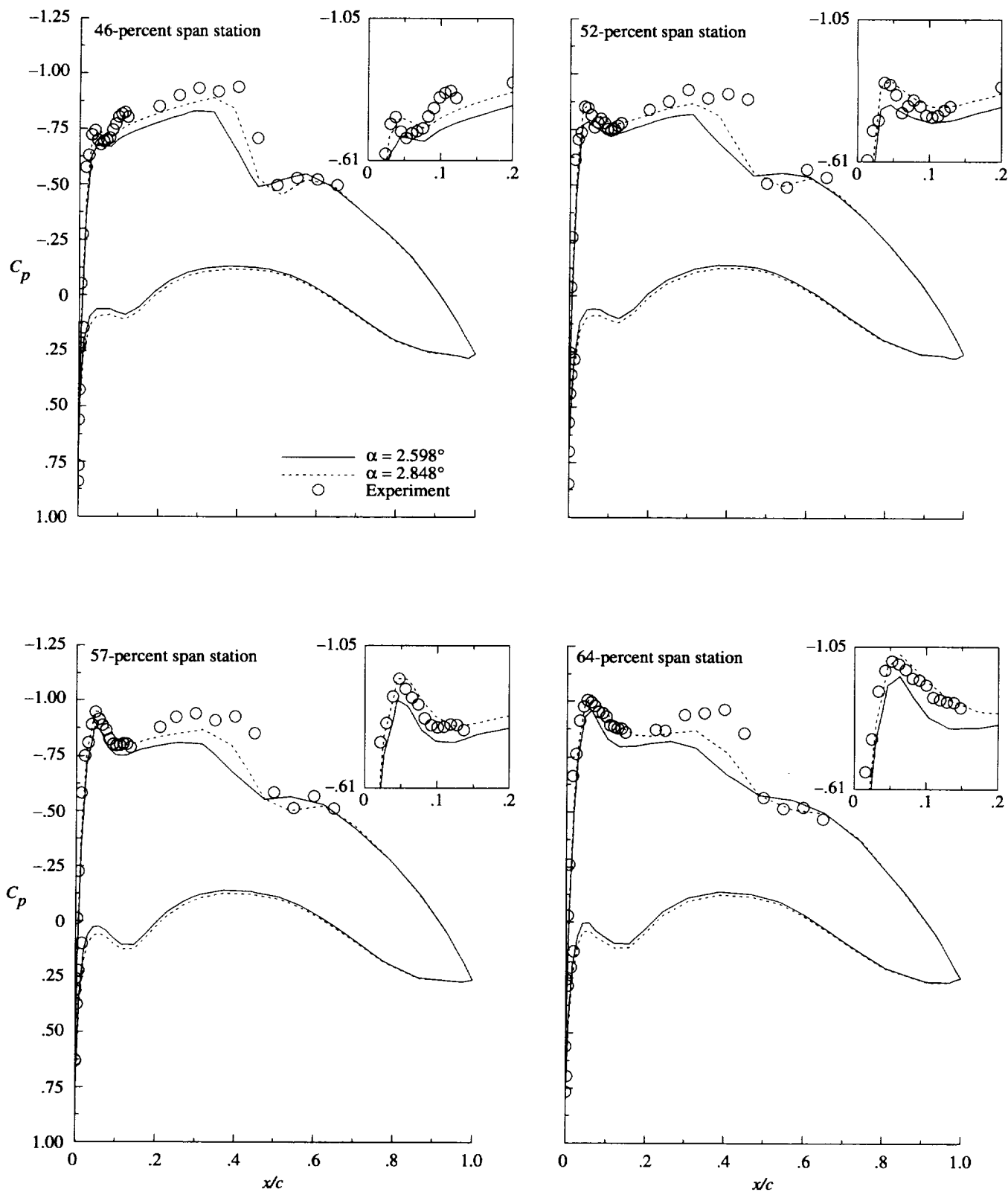
Figure 11. Effect of potential experimental angle-of-attack error on surface pressure coefficient distribution on grid 1 ($M = 0.793$; $\alpha = 2.598°$; $R = 31.9 \times 10^6$; 10 IBL stations).
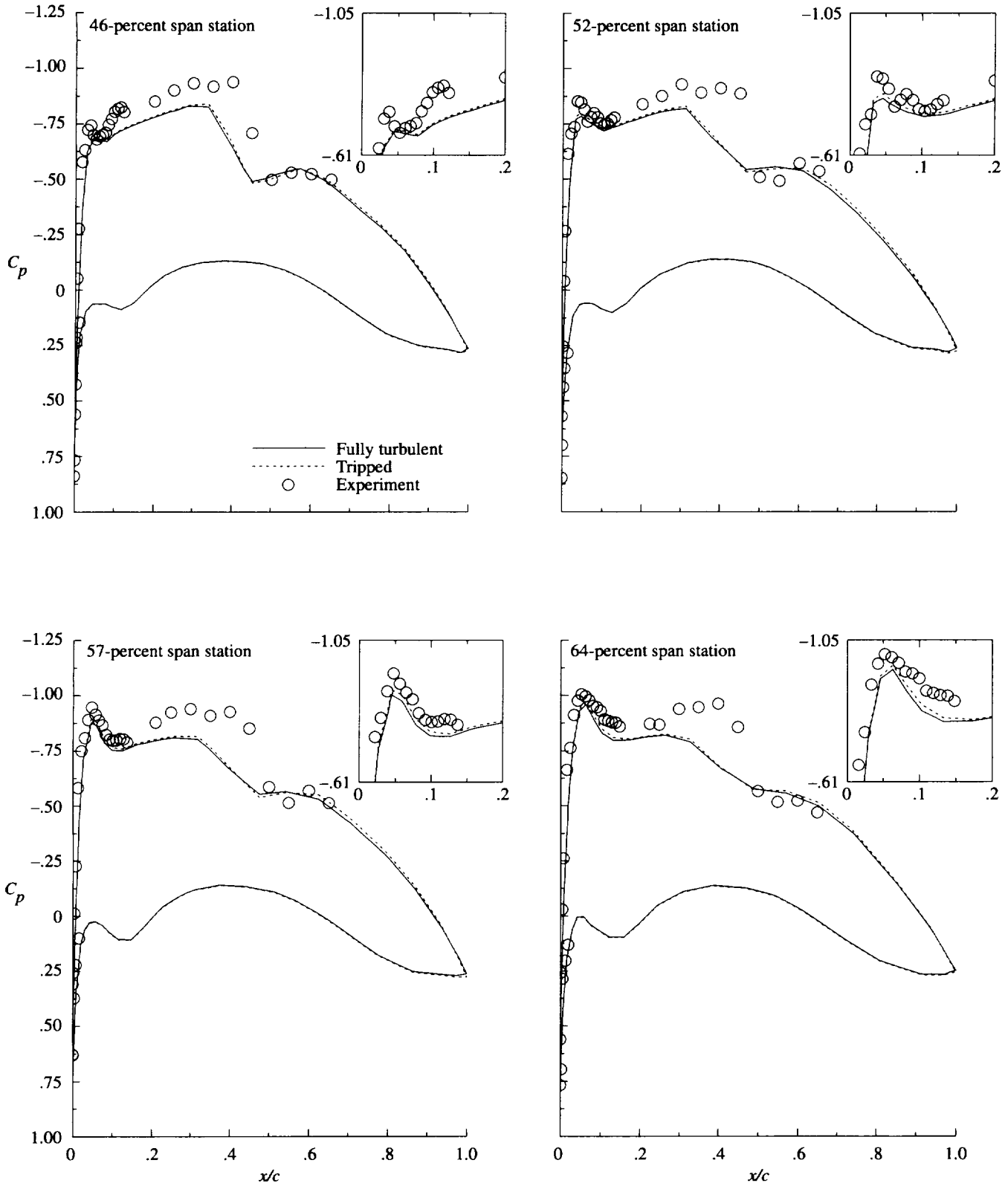
Figure 12. Effect of specification of transition on surface pressure coefficient distribution on grid 1 ($M = 0.793$; $\alpha = 2.598°$; $R = 31.9 \times 10^6$; 10 IBL stations). Transition is specified between 42 percent and 47 percent chord for tripped case.
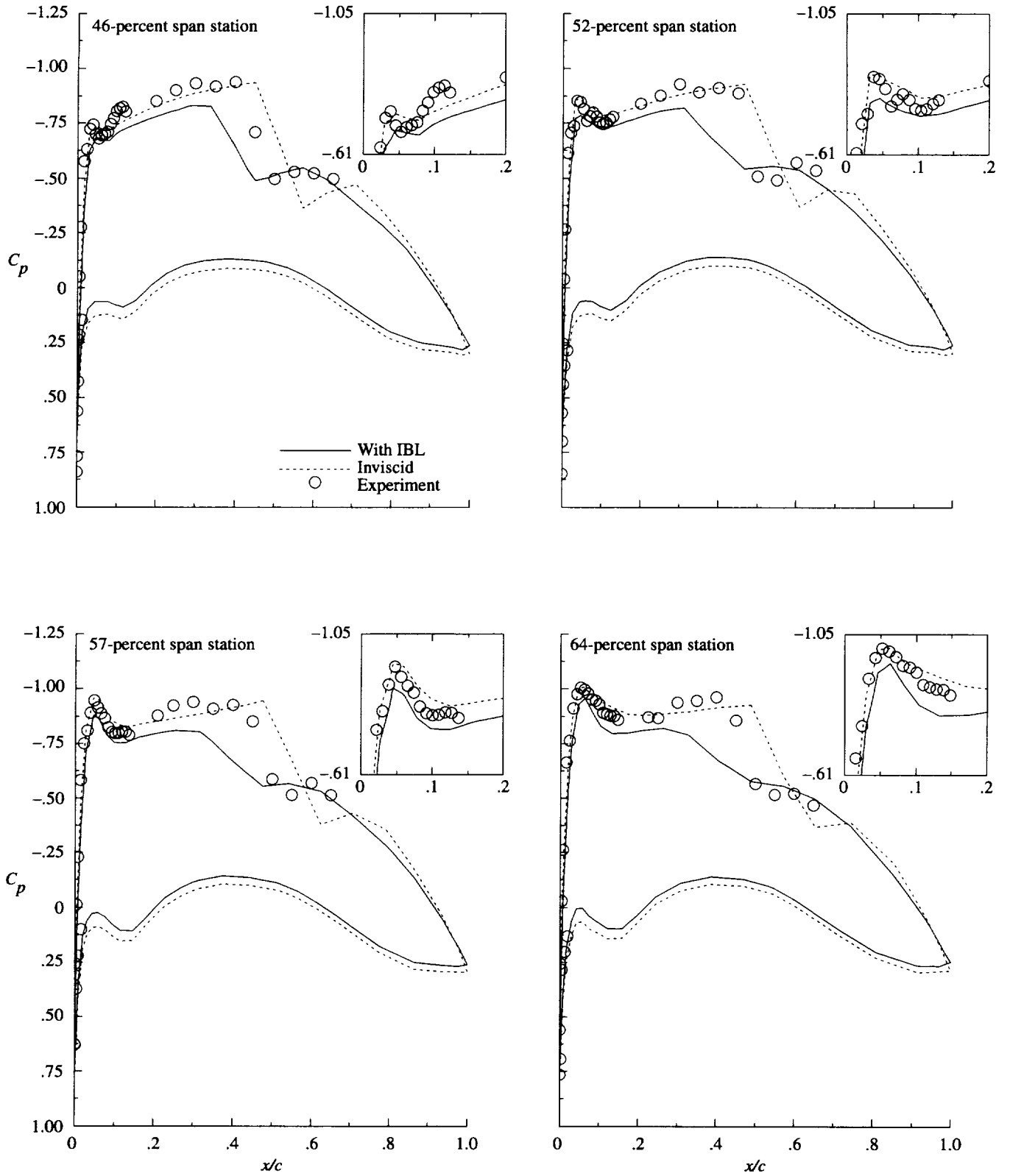
Figure 13. Comparison of surface pressure coefficient with experiment for both an inviscid computation and a computation with interactive boundary layer on grid 1 ($M = 0.793$; $\alpha = 2.598°$; $R = 31.9 \times 10^6$; 10 IBL stations).
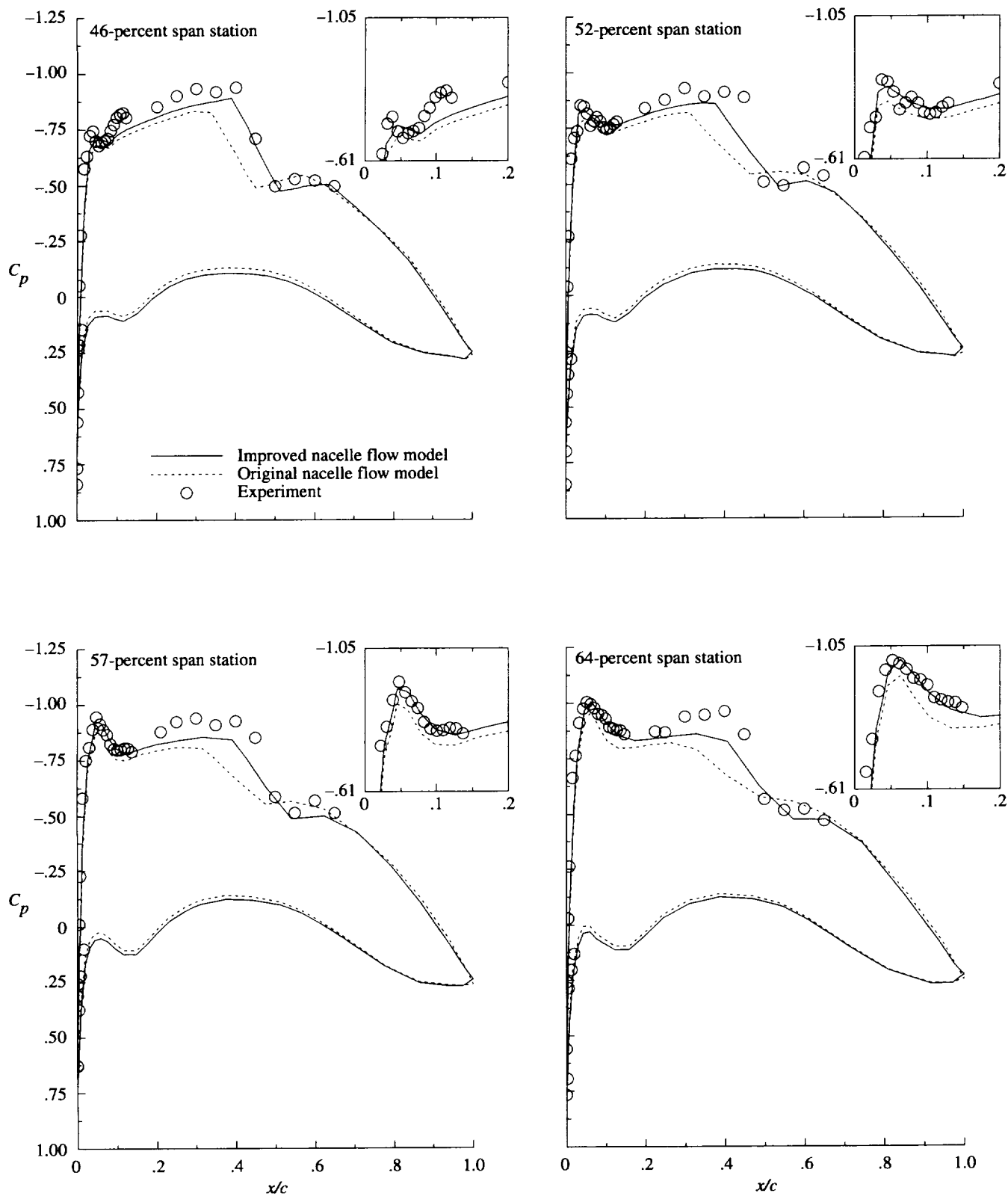
Figure 14. Comparison of surface pressure coefficient with experiment for results from two versions of nacelle inflow/outflow boundary conditions on grid 1 ($M = 0.793$; $\alpha = 2.598°$; $R = 31.9 \times 10^6$; 10 IBL stations).
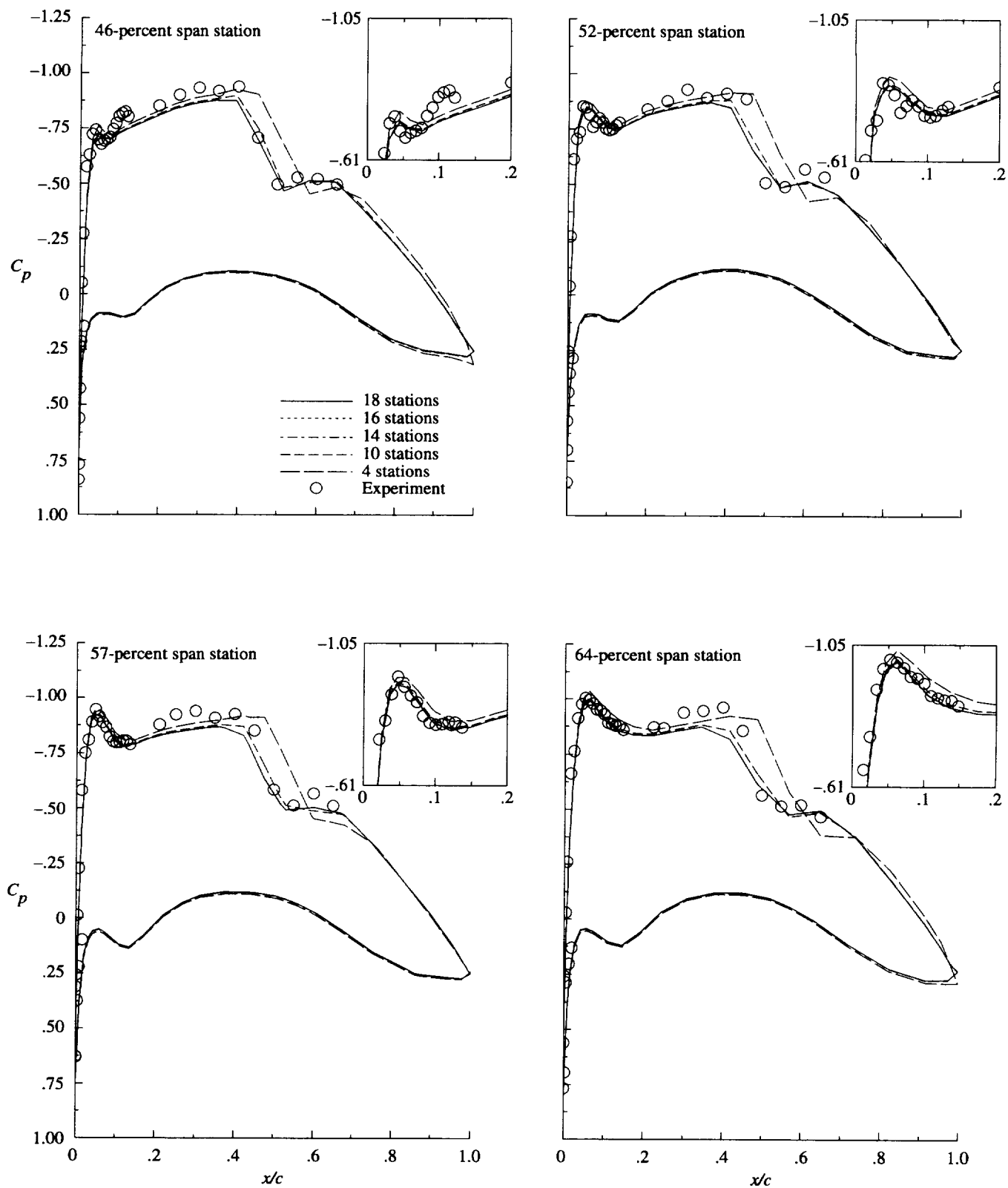
Figure 15. Effect of number of boundary-layer stations on surface pressure coefficient distribution on grid 2 (M = 0.793; α = 2.598°; R = 31.9 × 10^6). Calculations for 14 and 16 IBL stations are indistinguishable from 18-station calculation.
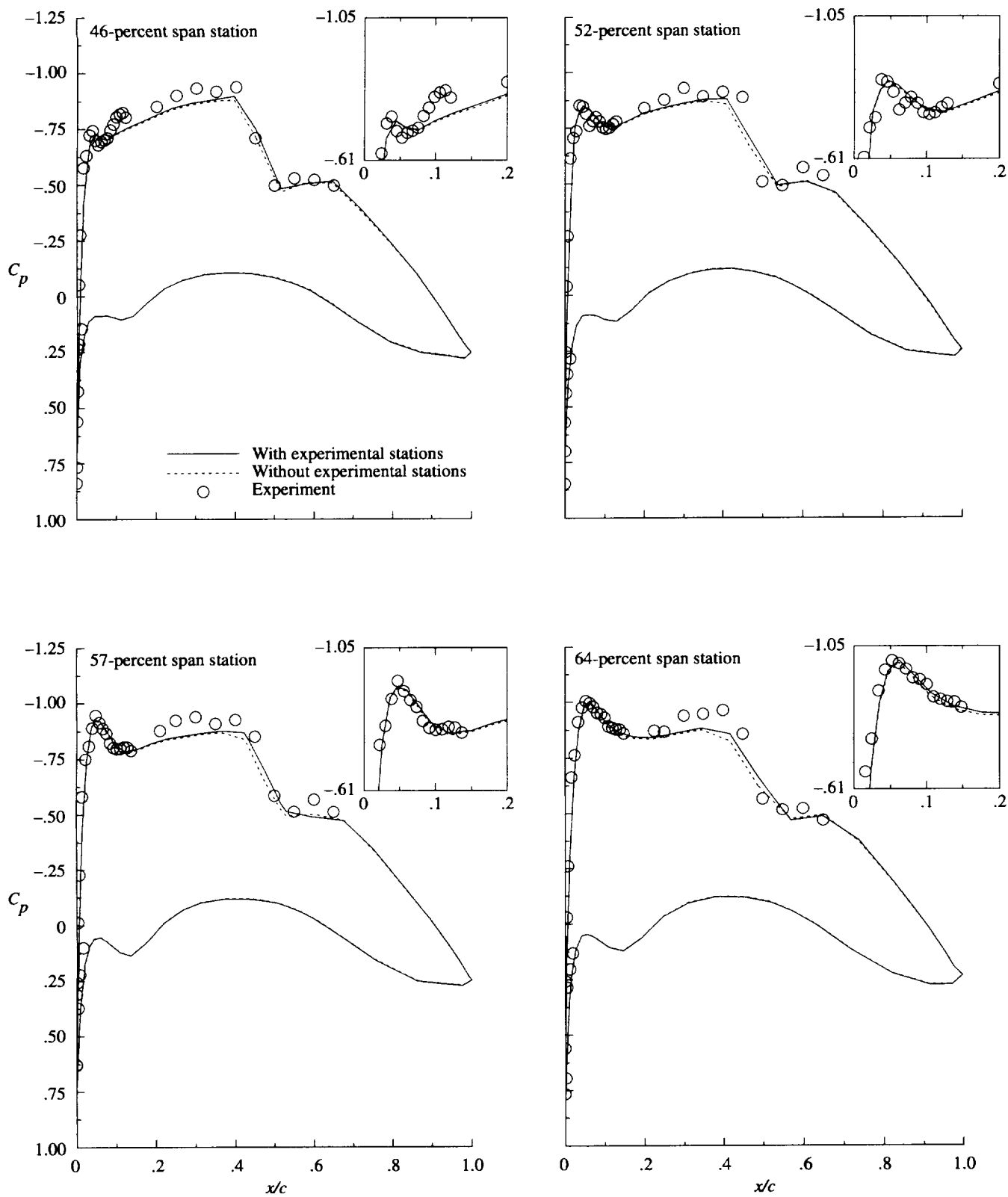
Figure 16. Effect of boundary layer station placement on surface pressure coefficient for grid 2 with 10 IBL stations $(M = 0.793; \alpha = 2.598°; R = 31.9 \times 10^6)$.
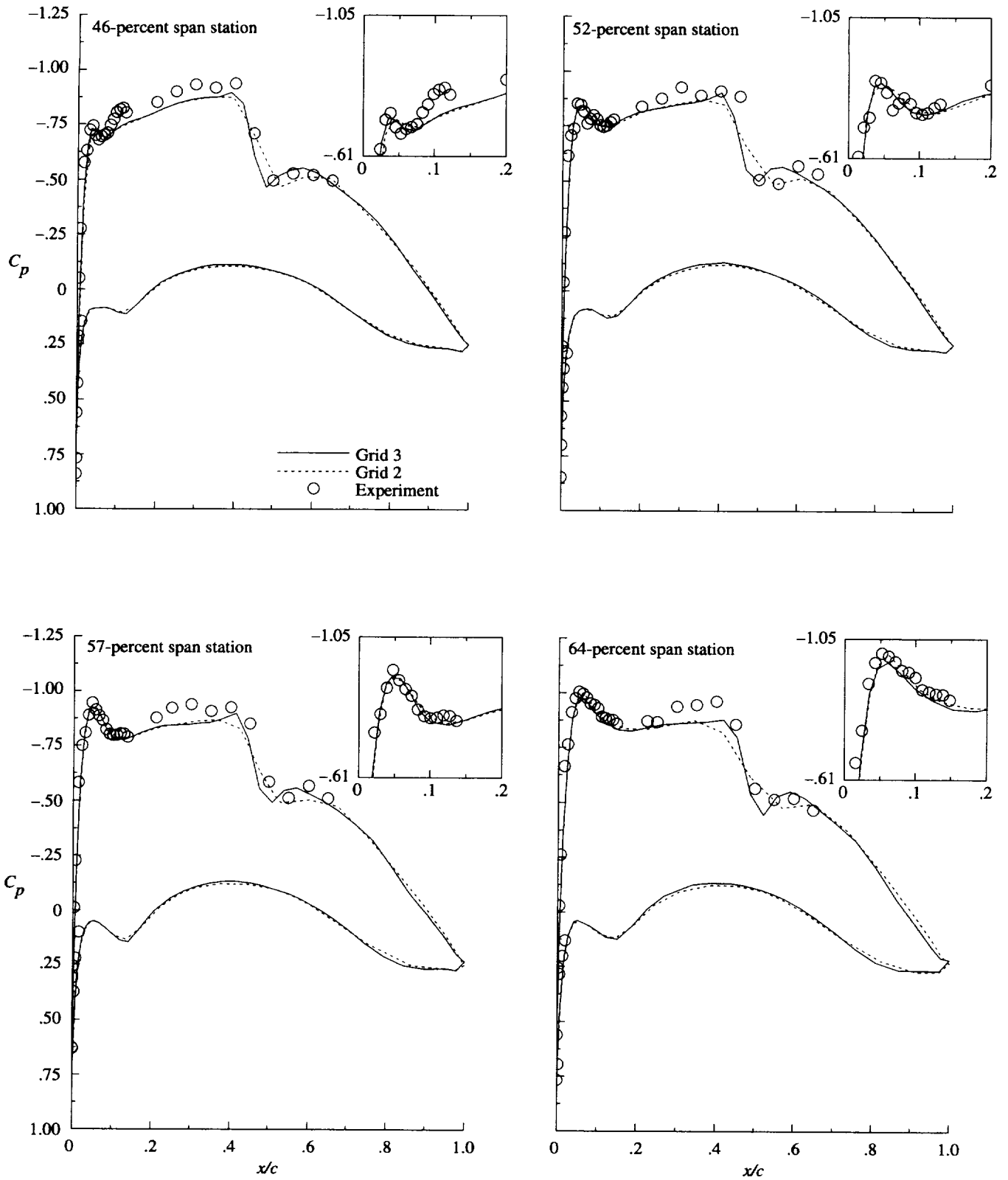
Figure 17. Comparison of surface pressure coefficient with experiment for grids 2 and 3 with 18 IBL stations ($M = 0.793$; $\alpha = 2.598°$; $R = 31.9 \times 10^6$).

Figure 18. Comparison of surface pressure coefficient with experiment for grids 3 and 4 ($M = 0.793$; $\alpha = 2.598°$; $R = 31.9 \times 10^6$; 18 IBL stations).

27
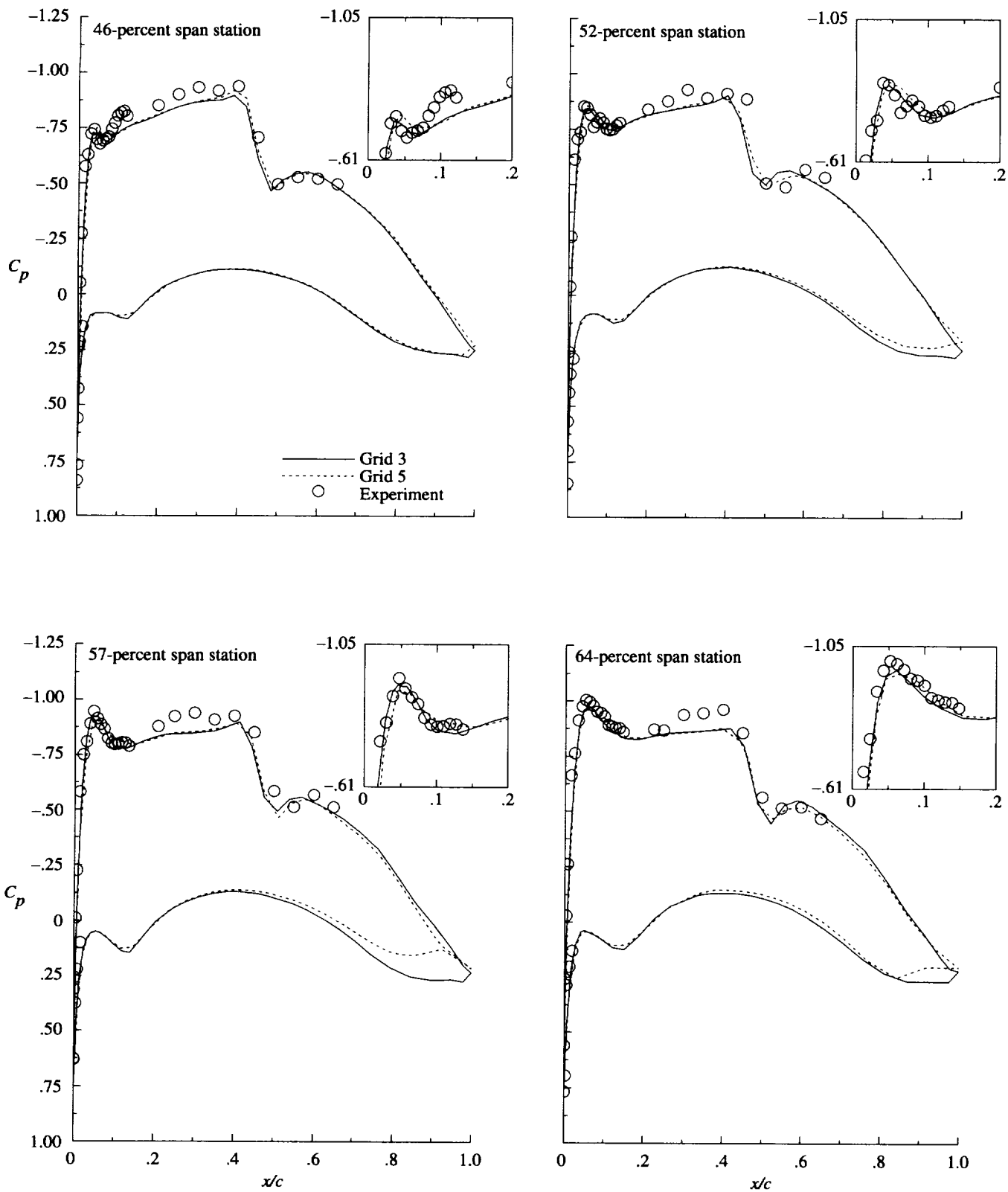
Figure 19. Comparison of surface pressure coefficient with experiment for grids 3 and 5 (M = 0.793; α = 2.598°; $R = 31.9 \times 10^6$; 18 IBL stations).
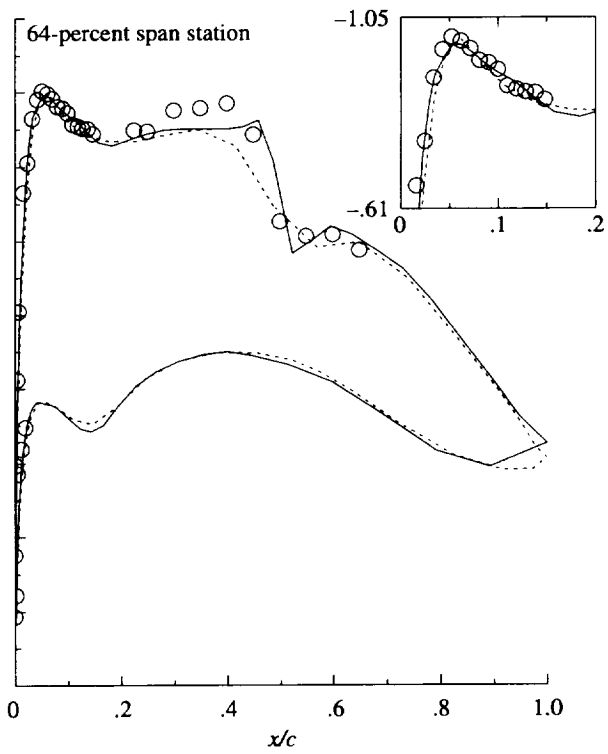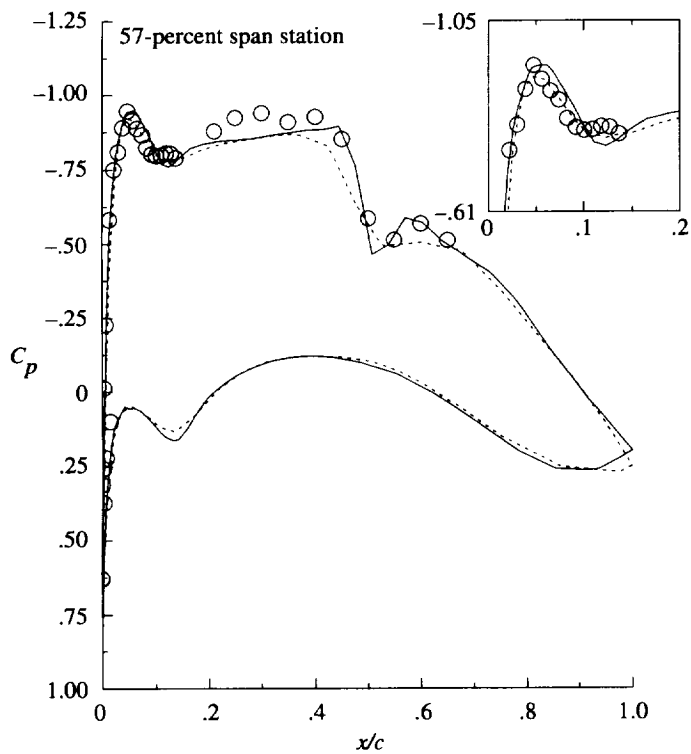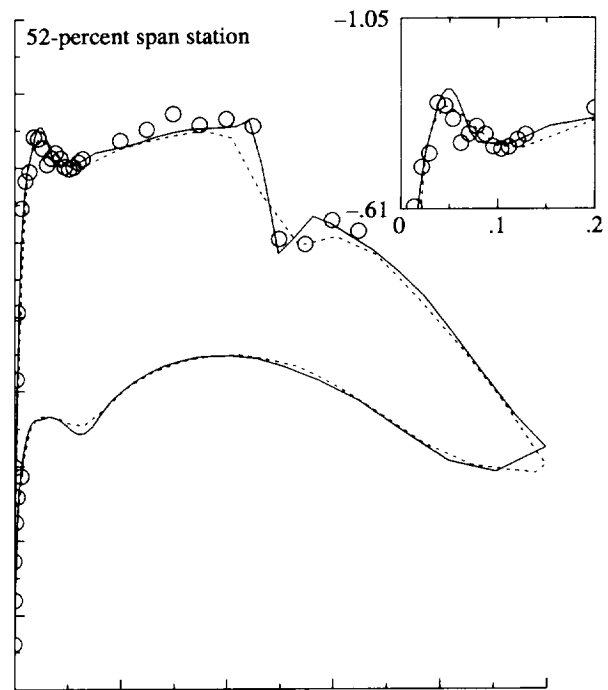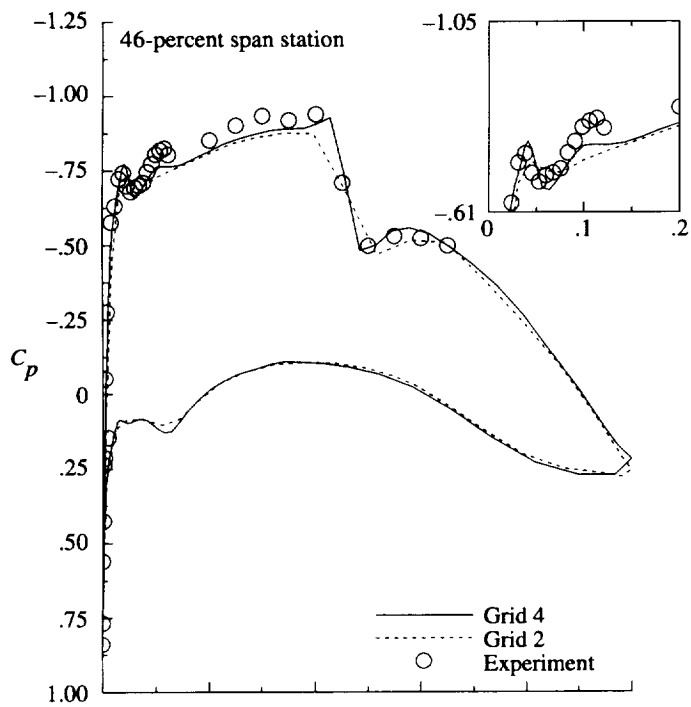
Figure 20. Overall effect of grid refinement comparison of calculations on grids 2 and 4 ($M = 0.793$; $\alpha = 2.598°$; $R = 31.9 \times 10^6$; 18 IBL stations).

29
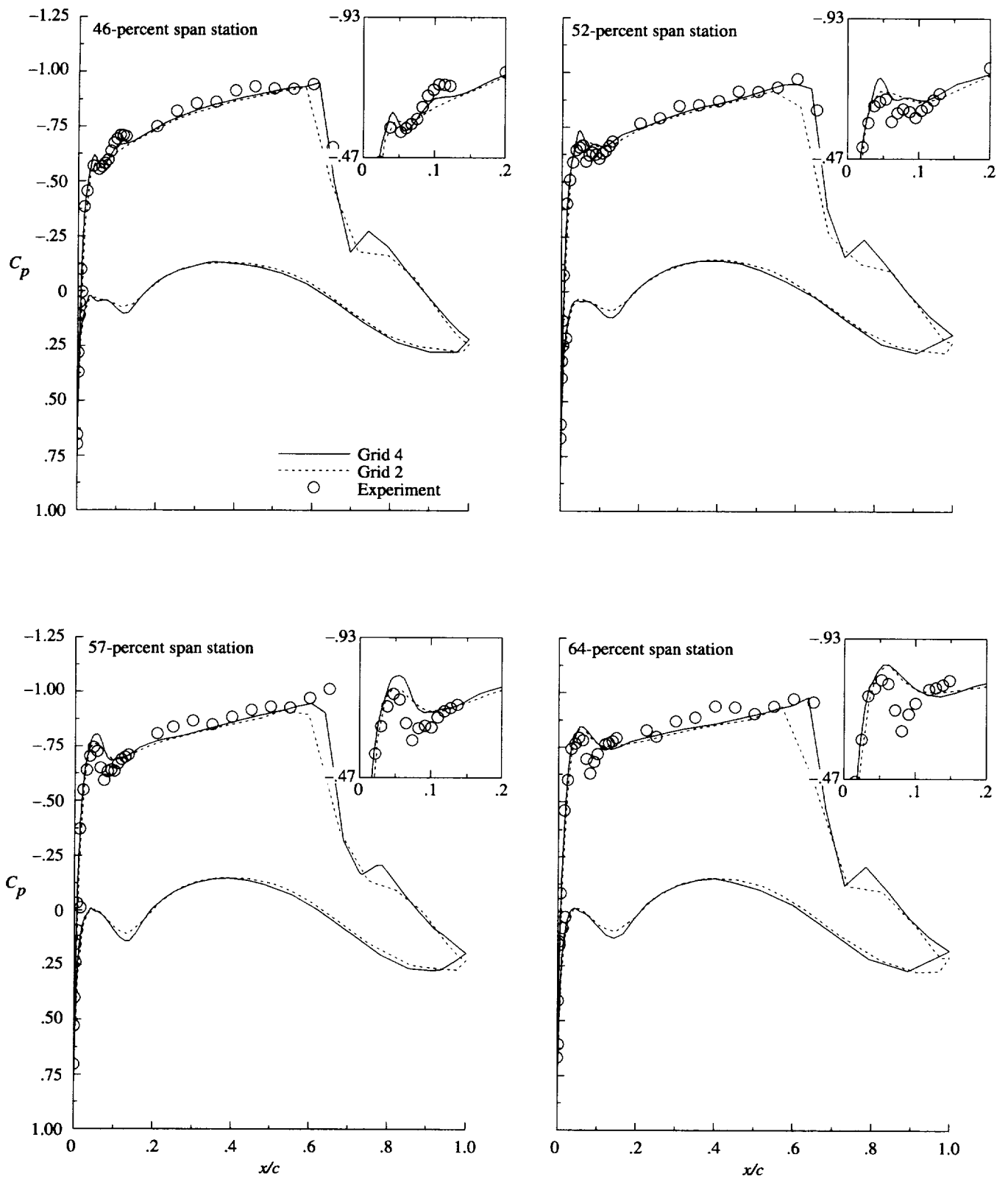
Figure 21. Overall effect of grid refinement comparison on grids 2 and 4 ($M = 0.820$; $\alpha = 2.377°$; $R = 30 \times 10^6$; 18 IBL stations).
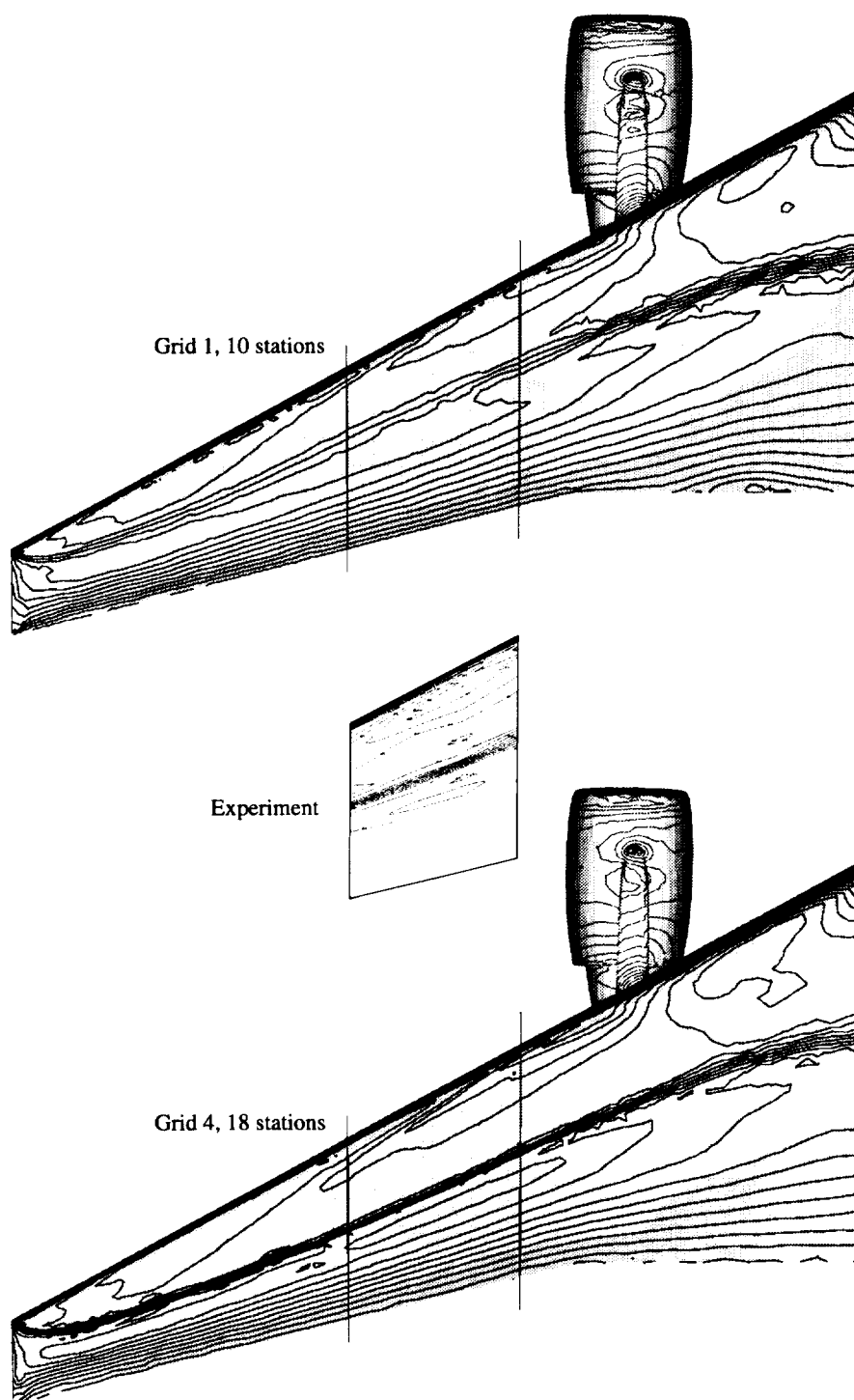
Figure 22. Upper surface isobars ($M = 0.793$; $\alpha = 2.598°$; $R = 31.9 \times 10^6$). Vertical hash marks indicate region of test pressure distribution measurements.
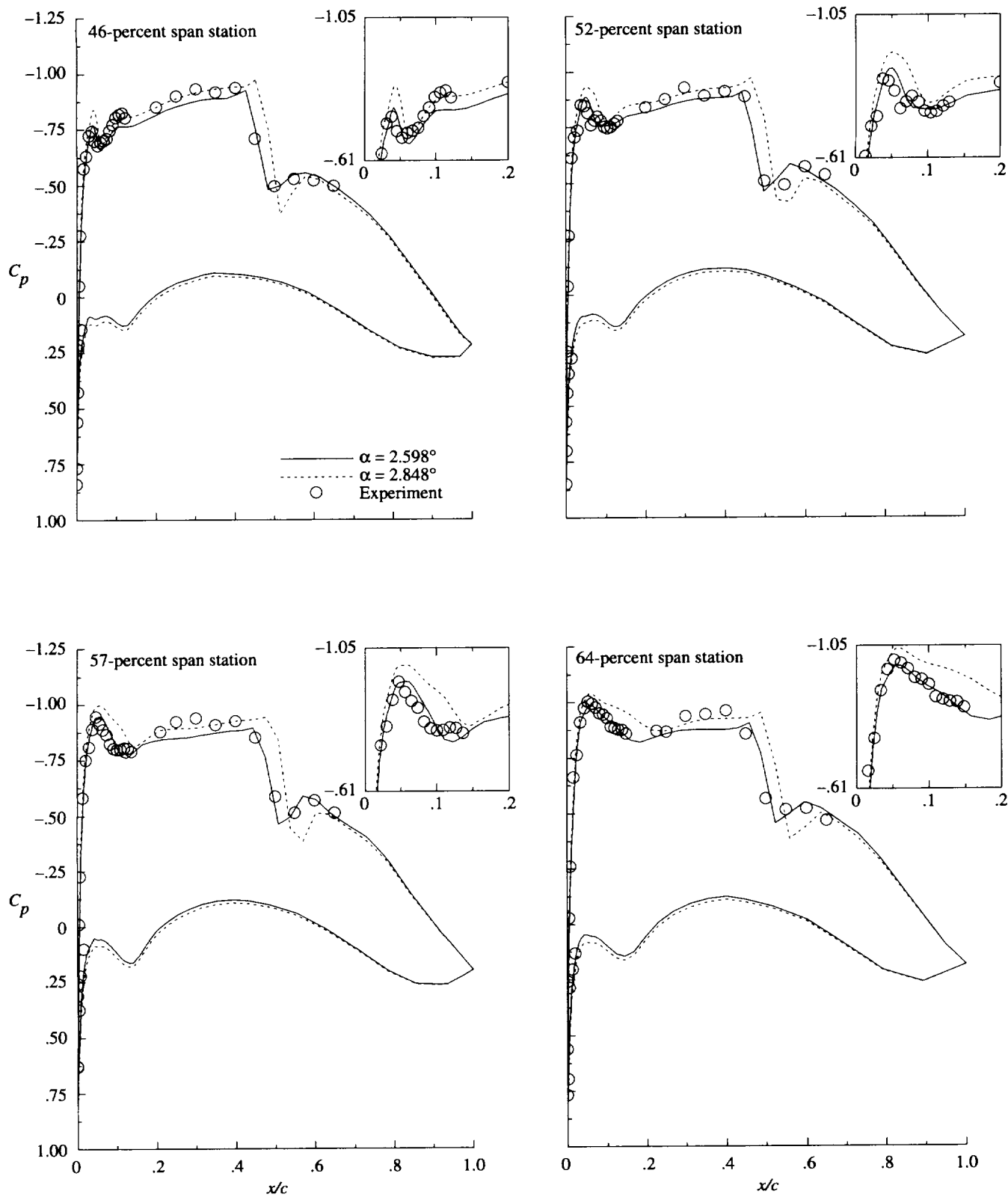
31
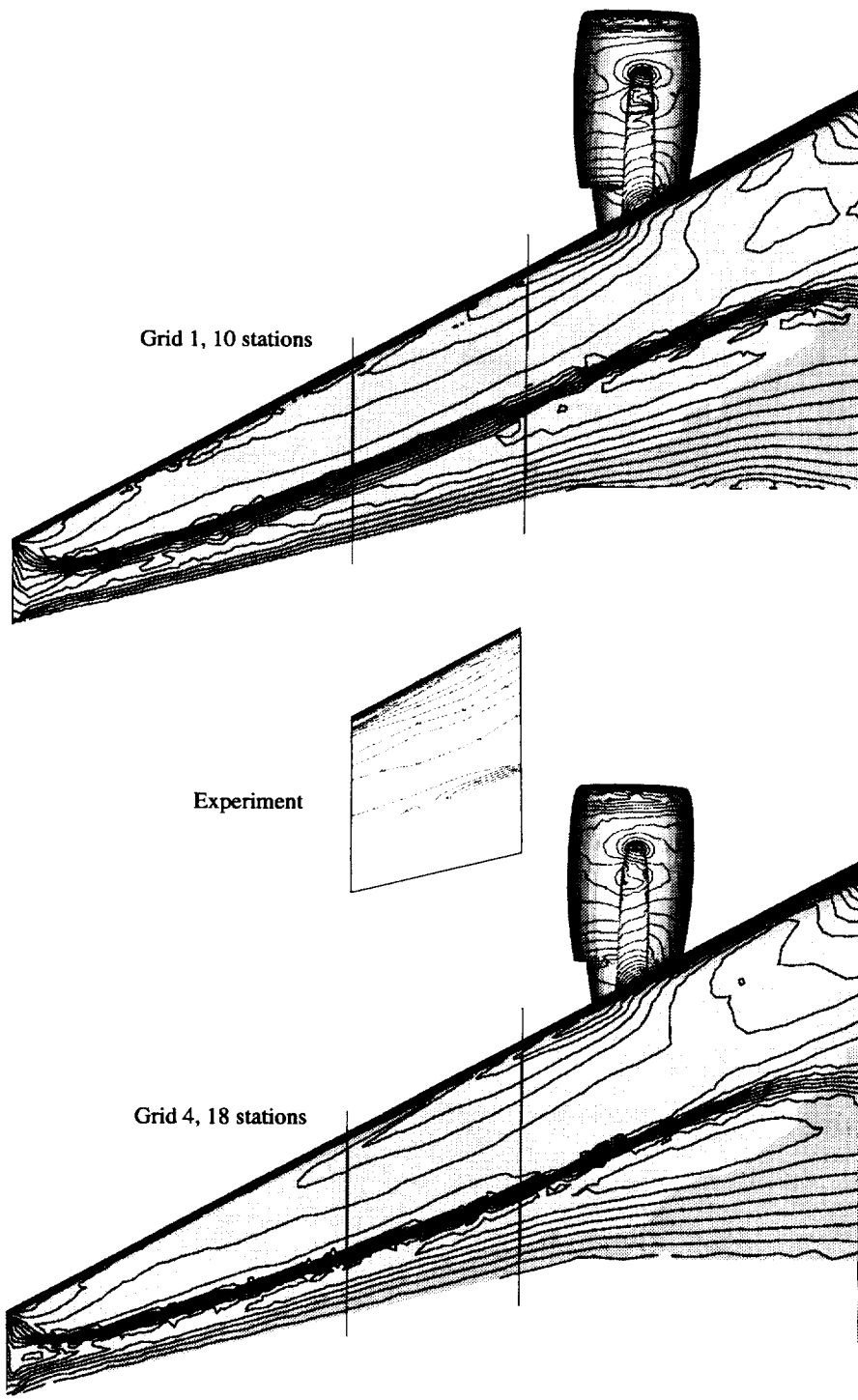
Figure 23. Upper surface isobars ($M = 0.820$; $\alpha = 2.377°$; $R = 30 \times 10^6$). Vertical hash marks indicate region of test pressure distribution measurements.

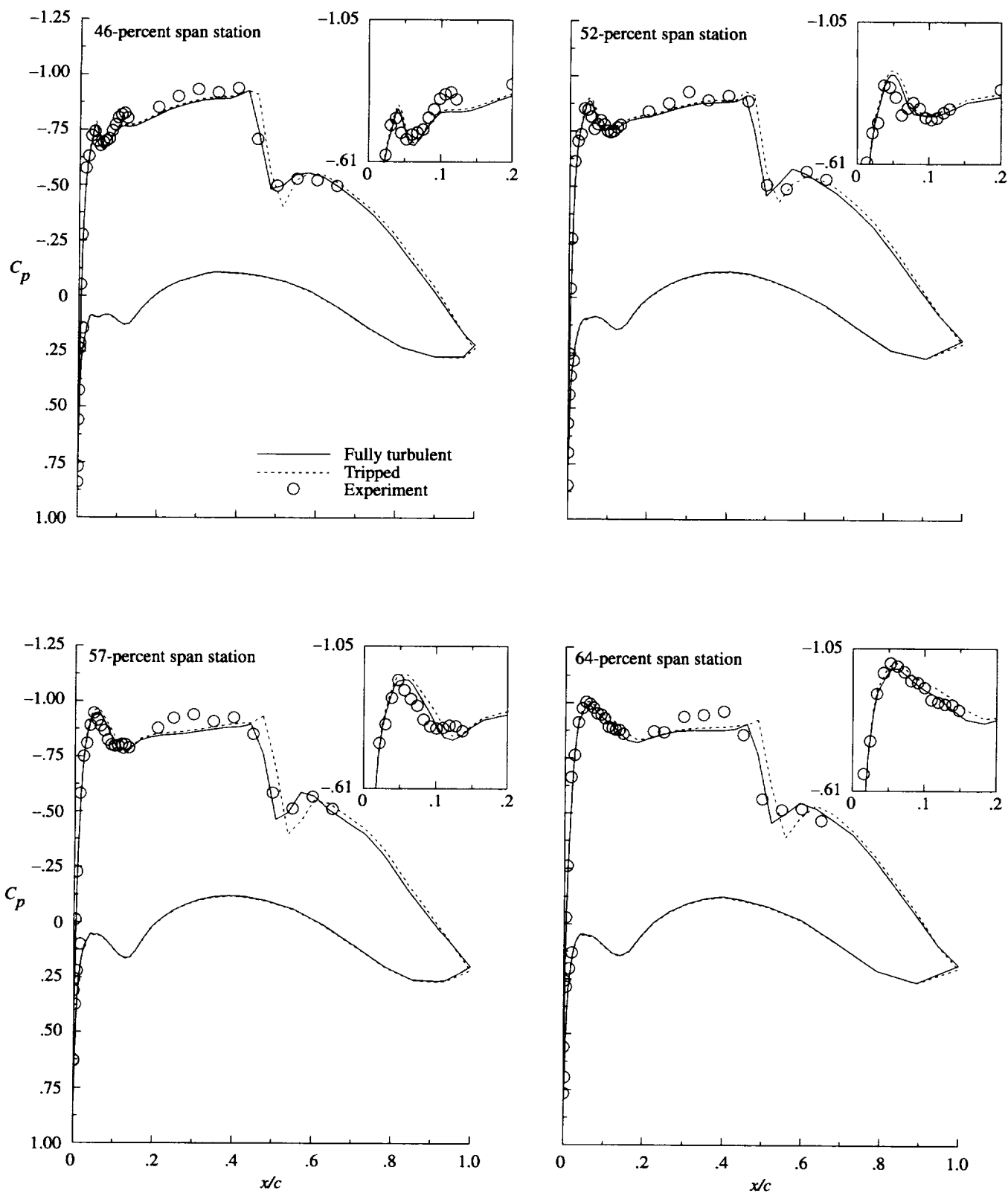Figure 24. Effect of uncertainty in angle of attack on finest grid (grid 4, 18 IBL stations), ($M = 0.793$; $\alpha = 2.598°$; $R = 31.9 \times 10^6$).

Figure 25. Effect of specification of transition location on finest grid (grid 4, 18 IBL stations), ($M = 0.793$; $\alpha = 2.598°$; $R = 31.9 \times 10^6$).
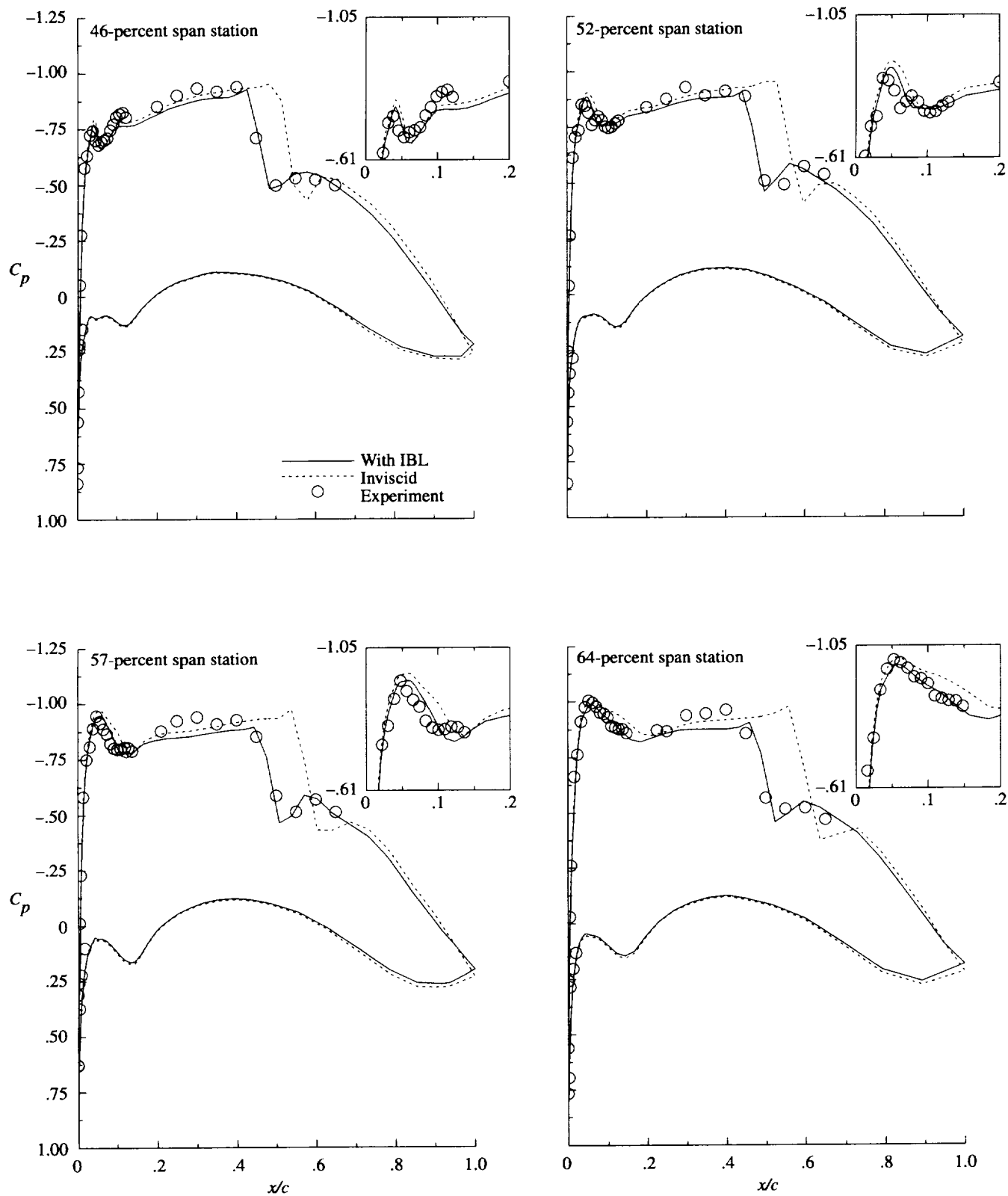
Figure 26. Effect of presence of boundary layer on finest grid (grid 4, 18 IBL stations), (M = 0.793; α = 2.598°; R = 31.9 × 10⁶).
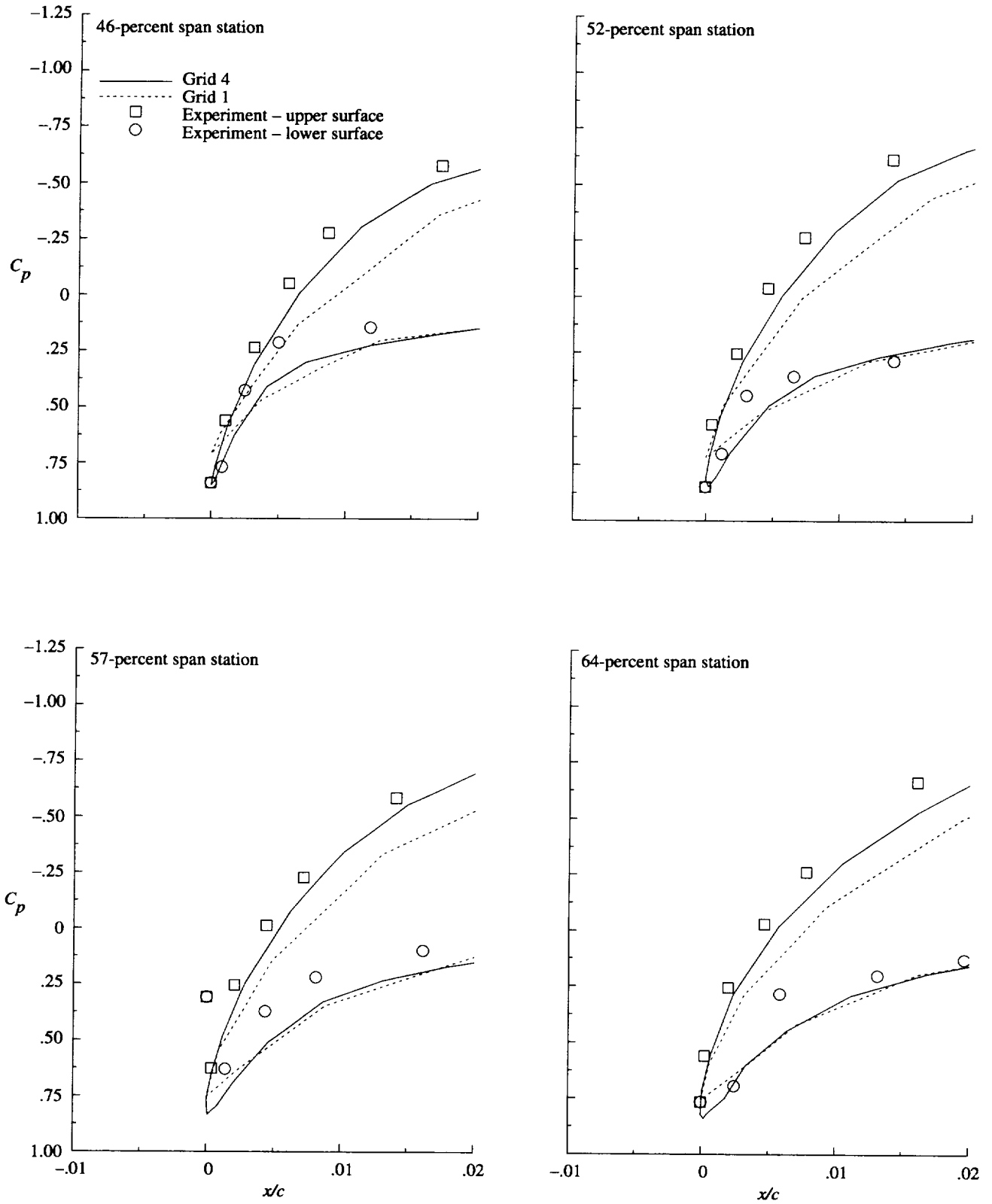
Figure 27. Comparison of experiment with theoretical attachment line location from grid 1 (10 IBL stations) and grid 4 (18 IBL stations); (M = 0.793; α = 2.598°; R = 31.9 × 10⁶).
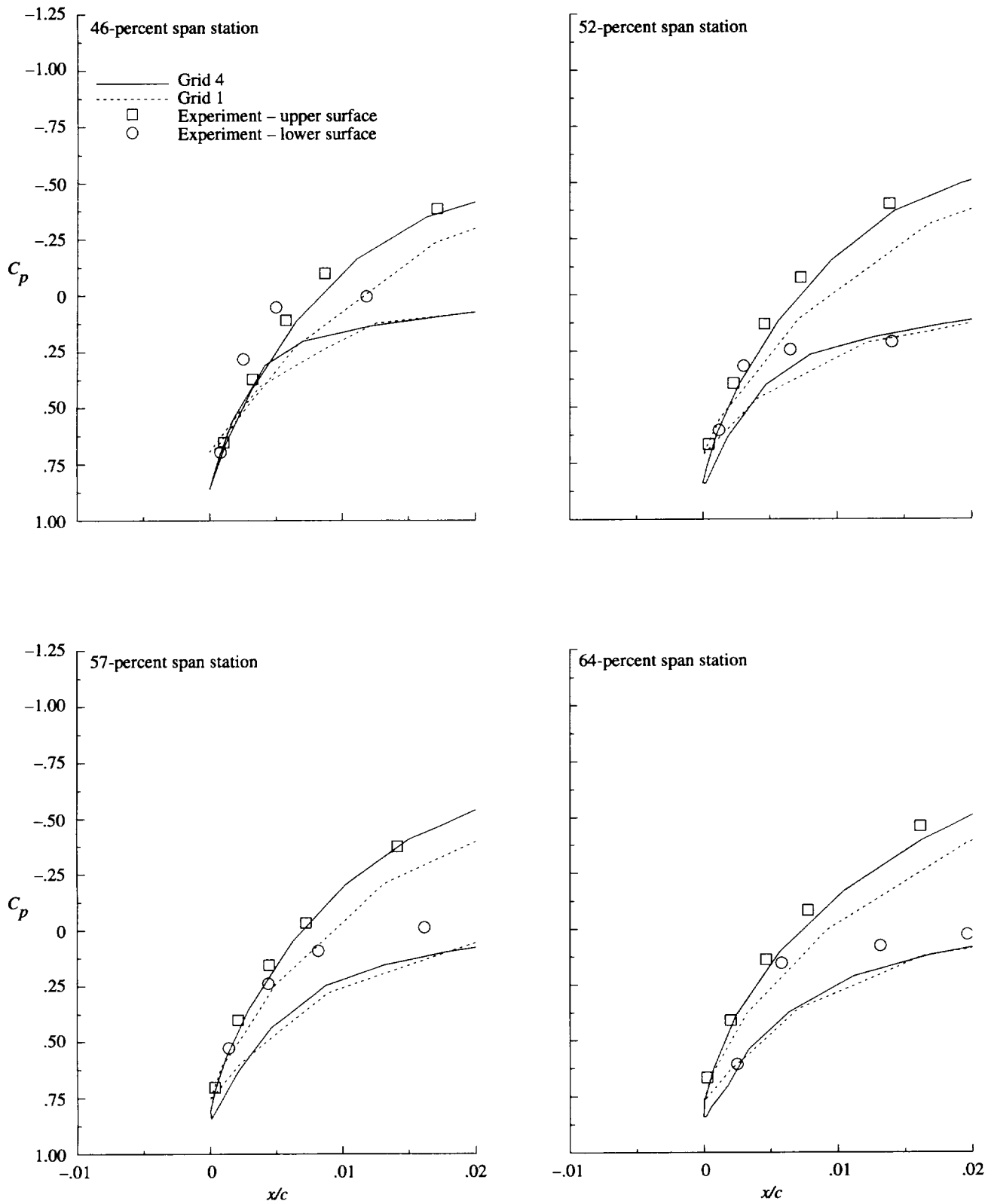
Figure 28. Comparison of experiment with theoretical attachment line location from grid 1 (10 IBL stations) and grid 4 (18 IBL stations); ($M = 0.820$; $\alpha = 2.377°$; $R = 30 \times 10^6$).

37

REPORT DOCUMENTATION PAGE

1. AGENCY USE ONLY (Leave blank)	2. REPORT DATE August 1998	3. REPORT TYPE AND DATES COVERED Technical Publication

4. TITLE AND SUBTITLE
Assessment of an Euler-Interacting Boundary Layer Method Using High Reynolds Number Transonic Transport Flight Data

5. FUNDING NUMBERS
WU 522-11-51-02

6. AUTHOR(S)
Daryl L. Bonhaus and Dal V. Maddalon

7. PERFORMING ORGANIZATION NAME(S) AND ADDRESS(ES)
NASA Langley Research Center
Hampton, VA 23681-2199

8. PERFORMING ORGANIZATION REPORT NUMBER
L-17626

9. SPONSORING/MONITORING AGENCY NAME(S) AND ADDRESS(ES)
National Aeronautics and Space Administration
Washington, DC 20546-0001

10. SPONSORING/MONITORING AGENCY REPORT NUMBER
NASA/TP-1998-208461

11. SUPPLEMENTARY NOTES

12a. DISTRIBUTION/AVAILABILITY STATEMENT
Unclassified–Unlimited
Subject Category 02   Distribution: Standard
Availability: NASA CASI (301) 621-0390

12b. DISTRIBUTION CODE

13. ABSTRACT (Maximum 200 words)
Flight-measured high Reynolds number turbulent-flow pressure distributions on a transport wing in transonic flow are compared to unstructured-grid calculations to assess the predictive ability of a three-dimensional Euler code (USM3D) coupled to an interacting boundary layer module. The two experimental pressure distributions selected for comparative analysis with the calculations are complex and turbulent but typical of an advanced technology laminar flow wing. An advancing front method (VGRID) was used to generate several tetrahedral grids for each test case. Initial calculations left considerable room for improvement in accuracy. Studies were then made of experimental errors, transition location, viscous effects, nacelle flow modeling, number and placement of spanwise boundary layer stations, and grid resolution. The most significant improvements in the accuracy of the calculations were gained by improvement of the nacelle flow model and by refinement of the computational grid. Final calculations yield results in close agreement with the experiment. Indications are that further grid refinement would produce additional improvement but would require more computer memory than is available. The appendix data compare the experimental attachment line location with calculations for different grid sizes. Good agreement is obtained between the experimental and calculated attachment line locations.

14. SUBJECT TERMS
High Reynolds number; Hybrid laminar-flow control; Transonic flow; Wing design; Unstructured grid

15. NUMBER OF PAGES
43

16. PRICE CODE
A03

17. SECURITY CLASSIFICATION OF REPORT Unclassified	18. SECURITY CLASSIFICATION OF THIS PAGE Unclassified	19. SECURITY CLASSIFICATION OF ABSTRACT Unclassified	20. LIMITATION OF ABSTRACT